Master's Thesis
Degree Programme in Physics

Coupling between First Sound and Second Sound in ^{3}He - Superfluid ^{4}He Mixtures

Tapio Riekki

27.10.2015

Supervisors: Doc. Juha Tuoriniemi
D.Sc. Matti Manninen
Examiners: Doc. Juha Tuoriniemi
Prof. Jyrki Räisänen

UNIVERSITY OF HELSINKI
DEPARTMENT OF PHYSICS
P.O.Box 64 (Gustaf Hällströmin katu 2)
00014 University of Helsinki

HELSINGIN YLIOPISTO
HELSINGFORS UNIVERSITET
UNIVERSITY OF HELSINKI

Tiedekunta/Osasto Fakultet/Sektion – Faculty	Laitos/Institution– Department
Faculty of Science	Department of Physics

Tekijä/Författare – Author
Tapio Riekki

Työn nimi / Arbetets titel – Title
Coupling between First Sound and Second Sound in ^{3}He – Superfluid ^{4}He Mixtures

Oppiaine /Läroämne – Subject
Physics

Työn laji/Arbetets art – Level	Aika/Datum – Month and year	Sivumäärä/ Sidoantal – Number of pages
Master's Thesis	October 2015	52

Tiivistelmä/Referat – Abstract

Helium has two stable isotopes: more common ^{4}He with four nucleons, and the very rare ^{3}He with three nucleons. At sufficiently low temperature, helium can become superfluid that has no viscosity. This transition is quantum mechanical in nature, and since bosonic ^{4}He and fermionic ^{3}He follow different quantum statistics, there is a significant difference in the transition temperature between them. It is about 2 K for pure ^{4}He, but for pure ^{3}He it is three orders of magnitude lower, around 1 mK.

^{3}He – ^{4}He mixtures also have several interesting properties at very low temperatures, such as the finite solubility of ^{3}He in ^{4}He even at absolute zero limit. However, at kelvin range, where our experiment took place, the notable feature is the shifting of the supefluid transition temperature of ^{4}He to a lower temperature due to addition of ^{3}He.

Bulk superfluid helium can support two different sound modes: first sound is ordinary pressure (or density) wave, whereas second sound is a temperature (or entropy) wave, unique to superfluid systems. In inviscid superfluid systems, temperature fluctuations can propagate as second sound wave, but in normal systems, on the other hand, this is not possible, as all temperature fluctuations are strongly damped. First sound and second sound do not usually exist independent of each other, rather pressure variations are accompanied by variations in temperature, and vice versa.

In this thesis, we studied experimentally the coupling between first and second sound in dilute ^{3}He - superfluid ^{4}He mixtures, at saturated vapor pressure, at temperatures between 2.2 K and 1.7 K, and at ^{3}He concentrations ranging from 0 % to 11%, using a quartz tuning fork mechanical oscillator. Second sound that is coupled to first sound can create anomalies in the resonance response of the quartz tuning fork, so-called second sound resonances. We learned that there exists a temperature and concentration region, where these anomalies disappear, which would indicate two sound modes decoupling from each other. We also present a hydrodynamical model that correctly predicts the decoupling behavior.

Avainsanat – Nyckelord – Keywords
Superfluid, ^{3}He – ^{4}He mixture, Second sound

Säilytyspaikka – Förvaringställe – Where deposited
Kumpula Campus Library

Muita tietoja – Övriga uppgifter – Additional information

HELSINGIN YLIOPISTO
HELSINGFORS UNIVERSITET
UNIVERSITY OF HELSINKI

Tiedekunta/Osasto Fakultet/Sektion – Faculty	Laitos/Institution– Department	
Matemaattis-luonnontieteellinen	Fysiikan laitos	
Tekijä/Författare – Author		
Tapio Riekki		
Työn nimi / Arbetets titel – Title		
Coupling between First Sound and Second Sound in ^{3}He – Superfluid ^{4}He Mixtures		
Oppiaine /Läroämne – Subject		
Fysiikka		
Työn laji/Arbetets art – Level	Aika/Datum – Month and year	Sivumäärä/ Sidoantal – Number of pages
Pro gradu -tutkielma	Lokakuu 2015	52

Tiivistelmä/Referat – Abstract

Heliumilla on kaksi stabiilia isotooppia: yleisemmällä ^{4}He on ytimessään neljä hiukkasta, kun taas hyvin harvinaisella ^{3}He on vain kolme. Tarpeeksi matalassa lämpötilassa helium voi muuttua supranesteeksi, jolloin esimerkiksi sen viskositeetti katoaa kokonaan. Supranestetransitio on luonteeltaan kvanttimekaaninen, joten koska ^{4}He on bosoni ja ^{3}He fermioni, niiden on noudatettavaa eri kvanttistatistikkaa. Sen vuoksi supranestetransitiolämpötilassa on huomattava ero: puhtalla ^{4}He se on noin 2 K, kun taas puhtalla ^{3}He se on kolme kertaluokkaa matalampi noin 1 mK

^{3}He - ^{4}He -seoksilla on myös useita mielenkiintoisia ominaisuuksia, kuten ^{3}He äärellinen liukoisuus ^{4}He:ään jopa absoluuttisen nollapisteen rajalla. Tässä tutkielmassa esiteltävät mittaukset on kuitenkin suoritettu noin yhden kelvinin lämpötilassa, jossa eräs seosten havaittava piirre on ^{4}He supranestetransition siirtyminen matalammalle lämpötilalle ^{3}He määrää kasvatettaessa.

Supraneste-heliumissa voi edetä kaksi erilaistä ääniaaltotyyppiä: tavallisen paineaallon (tai tiheysaallon) eli ensimmäisen äänen lisäksi löytyy lämpötila-aalto (tai entropia-aalto), jota kutsutaan toiseksi ääneksi. Toinen ääni on ainutlaatuinen supranestesysteemeille, koska viskoosittomassa supranesteessä lämpötilafluktuaatioiden on mahdollista edetä aaltomaisesti, kun taas normaaleissa systeemeissä ne ovat hyvin voimakkaasti vaimentuvia. Ensimmäinen ääni ja toinen ääni eivät yleensä esiinny toisistaan riippumatta vaan painevaihtelujen mukana tapahtuu lämpötilavaihteluja tai päinvastoin.

Tässä tutkielmassa on tarkasteltu kokeellisesti ensimmäisen ja toisen äänen kytkeytymistä toisiinsa laimeissa ^{3}He - supraneste ^{4}He -seoksissa kylläisessä höyrynpaineessa, lämpötilojen 2.2 K ja 1.7 K välillä sekä ^{3}He konsentraatioissa 0 %:sta aina 11 %:in käyttäen kvartsihaarukkavärähtelijää. Toinen ääni joka on kytkeytynyt ensimmäiseen ääneen pystyy aiheuttamaan poikkeamia kvartsihaarukan resonanssikäytökseen, joita kutsutaan toisen äänen resonansseiksi. Havaittiin, että tietyissä konsentraatioissa ja lämpötiloissa nämä poikkeamat katoavat, mikä kertoo kadonneesta kytkeytymisestä äänien välillä. Tutkielmassa esitellään myös hydrodynaaminen malli, joka ennustaa tämän kytkeytymisen häviämisen.

Avainsanat – Nyckelord – Keywords
supraneste, ^{3}He – ^{4}He -seos, toinen ääni

Säilytyspaikka – Förvaringställe – Where deposited
Kumpulan kampuskirjasto

Muita tietoja – Övriga uppgifter – Additional information

Contents

1 Introduction

The era of modern low temperature physics began in 1908, when Heike Kamerlingh Onnes managed to liquefy helium at 4.2 K, or at -268.95°C [1], opening up the Kelvin temperature range to science. In the following years outstanding discoveries were made. First, when mercury was cooled to liquid helium temperature, its electrical resistance suddenly dropped to zero. This phenomenon is known as superconductivity. Then, after that, it was observed that liquid helium itself started to behave unexpectedly when cooled to 2.2 K. Helium had become superfluid, which can flow completely freely, without friction.

At room temperature, helium is one of the most trivial substances, since it is a chemically inert noble gas. But at low temperatures, it becomes one of the most intriguing research subjects, as it enables us to study the fundamental properties of quantum mechanical particles. Indeed, the peculiar behavior of liquid helium at low temperatures can only be explained through quantum mechanics, no analogy to classical mechanics exists. Helium is the only observable quantum liquid since it is the only substance that does not solidify under its saturated vapor pressure even at absolute zero temperature limit. To solidify liquid helium, the pressure would have to be more than 25 times the normal air pressure.

Helium has two stable isotopes, the more common ^{4}He that Kamerlingh Onnes was able to liquefy, and the extremely rare ^{3}He, which is produced in tritium (^{3}H) decay in nuclear reactions. At room temperature, both isotopes behave almost identically, as the only difference is in their mass. However, at low temperatures, their behavior is dramatically different, since they represent the two fundamental types of particles: bosons and fermions. To which group a particle belongs, depends on its spin. ^{4}He is made up from a pair of protons, neutrons, and electrons each, and since each pair consists of spin 1/2 particles, with opposite spin direction, the total spin of ^{4}He is an integer, 0, making it a boson. ^{3}He, on the other hand, is a fermion, since its total spin is 1/2 due to an unpaired neutron in the nucleus.

The difference between these two particle types becomes apparent, when we discuss the superfluid transition temperature. ^{4}He becomes superfluid already at 2.2 K, but the required temperature for superfluidity in ^{3}He is a thousand times lower, about 1 mK. When the temperature is lowered below 2.2 K, more and more ^{4}He bosons start occupy the lowest quantum mechanical energy state in a Bose-Einstein condensation-like phenomenon. However, contrary to the usual Bose-Einstein condensation, where at low enough temperature practically all particles are in the lowest energy state, in ^{4}He only about 10 % of the atoms can occupy the lowest energy state due to the stronger interaction between ^{4}He atoms than between ideal Bose particles. Fermionic ^{3}He, by contrast, has to follow the Pauli exclusion principle, which allows only two particles, with opposite spin, to occupy the same energy state. ^{3}He cannot then form a condensate same way as ^{4}He. Instead, it behaves more like the conduction electrons in superconductors: they form

so-called Cooper pairs, which, according to the BCS theory, can form the condensate. As the pair of fermions has an integer spin, the pair behaves like a boson. The sufficient condition for formation of Cooper pairs is an attractive interaction between the constituent particles; if there is an attraction between fermions, they will form Cooper pairs at some low enough temperature. For pure ^{3}He this temperature is around 1 mK. [2]

Mixtures of the two helium isotopes are also interesting research subjects. A remarkable feature of these mixtures, is the finite solubility of ^{3}He in ^{4}He even at absolute zero temperature limit, which, for example, makes it possible to cool liquid helium to millikelvin range. Furthermore, in dilute mixtures, the superfluid transition temperature of ^{4}He is suppressed to a lower temperature, and the superfluid transition of ^{3}He is expected to occur only at such low temperatures that have not been reached with current cooling methods. [3]

A peculiar feature of bulk superfluid helium is it being able to support two different sound modes. While first sound is an ordinary pressure (or density) wave, second sound is a mode unique to superfluid systems, a propagating temperature (or entropy) wave. In the non-superfluid systems, the temperature fluctuations are so strongly damped that there cannot exist a temperature wave. The superfluid, however, can flow without any friction, making this second sound mode possible. These two sound modes do not exist completely independent of each other, but rather variations in pressure are accompanied by variations in temperature and vice versa. The coupling between first sound and second sound has been studied in superfluid helium in aerogel by Brusov *et al.* [4], where they also present calculations of the sound coupling in bare ^{3}He$-^4$He mixtures. However, as pointed out by Rysti [5], they made an error in their calculations which prevented them from noticing an interesting property of the coupling between second and first sound. At some temperature and concentration region, the coupling vanishes, and the two sound modes become completely independent. The goal of our experiment was first to verify the existence of this decoupling region, and then to observe its properties. To do so, we studied ^{3}He $-$ ^{4}He mixtures, at temperatures between 2.2 K and 1.7 K, and at ^{3}He concentrations ranging from 0 % to 11 % using a quartz tuning fork oscillator. The resonance response of this fork would change depending on the coupling strength between first and second sound.

We start this thesis by talking a little more about general properties of ^{3}He $-$ ^{4}He mixtures, and then move on to theoretical calculations of the first and second sound velocities, as well as the coupling factors. After that, we describe our experimental setup, focusing on the quartz tuning fork oscillator, and before the results we shortly go over our experiment procedure, and finally sum up everything in the discussion section.

2 ^{3}He - ^{4}He Mixtures

The properties of ^{4}He are substantially modified by the addition of ^{3}He. Perhaps the most important property of these mixtures of two helium isotopes is the finite solubility of ^{3}He in ^{4}He even at absolute zero temperature limit, which, for example, enables us to cool the mixtures to millikelvin

temperatures. This, in turn, enables us to reach even lower temperatures using adiabatic nuclear demagnetization cooling [3]. In our experiment however, we remain still at relatively high temperature, and the important property that the addition of ^{3}He modifies, is the superfluid transition temperature of ^{4}He.

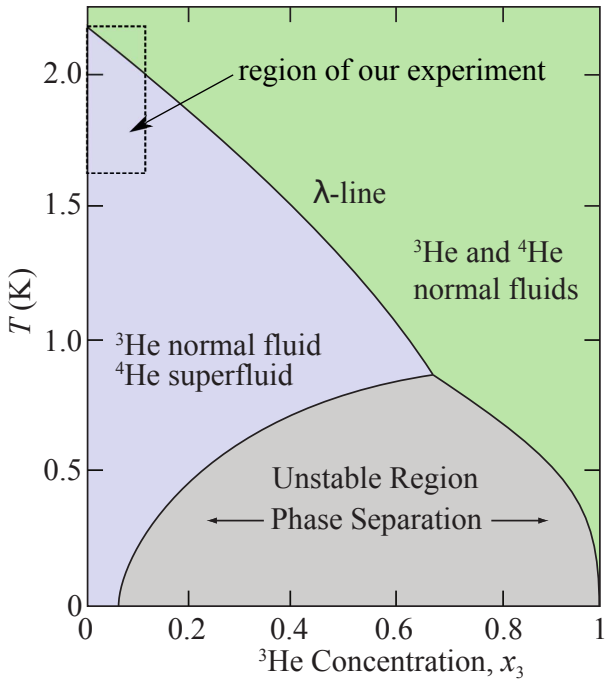

Figure 2.1: Low temperature phase diagram of liquid ^{3}He - ^{4}He mixtures at saturated vapor pressure. The region of our experiment is shown by the rectangle with dashed lines.

The phase diagram of liquid $^3\mathrm{He} - {}^4\mathrm{He}$ mixture is shown in fig. (2.1), where the molar ^{3}He concentration, x_3, is expressed as

$$x_3 = \frac{N_3}{N_3 + N_4}, \tag{2.1}$$

where N_3 and N_4 are the number of ^{3}He and ^{4}He atoms, respectively.

Pure ^{4}He becomes superfluid at 2.1768 K, and pure ^{3}He superfluid transition is not shown in the figure, since it occurs at millikelvin range. The addition of ^{3}He lowers the total density of the liquid, and keeps ^{4}He atoms further apart, shifting the ^{4}He superfluid transition to lower temperature. The superfluid transition temperature of ^{4}He, T_λ, follows the λ-line of fig. (2.1), which is practically linear in the temperature and concentration range of our experiment.

At $x_3 = 67.5\,\%$, at 0.87 K temperature, the λ-line ends, and below this point the liquid will separate into ^{3}He rich phase and ^{4}He rich phase. On the ^{3}He rich phase, ^{4}He does not anymore become superfluid. When the temperature is still lowered, the ^{3}He rich phase eventually becomes pure ^{3}He, but, remarkably, in the ^{4}He rich phase there is always a finite amount of ^{3}He, even at

zero temperature limit. ^{3}He is lighter than ^{4}He and therefore it also has a larger zero point energy. This means that a ^{3}He atom occupies a larger volume than a ^{4}He atom. Now, when we mix ^{3}He atoms with ^{4}He atoms, the ^{3}He atom feels a stronger interaction with neighboring ^{4}He atoms, since they, with their lower zero-point energy, can come closer to it than other ^{3}He atoms. Hence, ^{3}He atom is more strongly bound in mixture than it would be in pure ^{3}He, which results in the finite solubility. Then, we have to remember that since ^{3}He is a fermion, it has to follow the Pauli exclusion principle, and each ^{3}He atom added to the mixture would have to go to a successively higher energy state, and eventually the binding energy will be the same in pure ^{3}He and in mixture. This Fermi character limits the solubility of ^{3}He in ^{4}He to 6.6 % at zero temperature limit, for example. [3]

The finite solubility is the basis of the dilution refrigerator technology, in which ^{3}He from the ^{3}He rich phase is continuously mixed into the ^{4}He rich phase. The enthalpy difference between these phases is used to produce cooling power. This is the only available continuous cooling method down to 10 mK range.

The attraction between ^{3}He atoms in mixture consists of two effects: first there is a magnetic interaction between $1/2$ total spin ^{3}He atoms, which is also present in pure ^{3}He , and second, there is the density effect discussed above. Since there exists an attraction between ^{3}He atoms in mixture, they can form Cooper pairs also in mixture, meaning that at some ultra low temperature it is possible to find a phase where both ^{3}He and ^{4}He are in superfluid state. It would present an interesting new system with mixture of bosonic and fermionic superfluids. However, it has not yet been observed, as the superfluid transition point of ^{3}He in mixture occurs only at some temperature below 100 μK, which has not been reached with current cooling methods. Temperatures below this have been achieved, but they are the electron temperatures of copper nuclear demagnetization cryostats. Because the thermal boundary resistance increases dramatically with decreasing temperature, it becomes more and more difficult to thermalize the liquid helium sample to the temperature of its container. A new proposed cooling method would utilize adiabatic melting of pure ^{4}He crystal in liquid ^{3}He. As the two isotopes would then mix, this setup would produce cooling similarly to the dilution refrigerator, and now the cooling power would directly cool helium, and we would not have to worry about the thermal boundary resistance effects. [6]

At equal temperature, the vapor pressure of ^{3}He is larger than that of ^{4}He, as shown in fig. (2.2). This difference is can also be explained by the zero-point energy difference between the isotopes. This means that the ^{3}He concentration in the vapor above the mixture is large, even at low ^{3}He concentrations in the liquid. However, as the temperature is lowered the vapor pressure eventually becomes very small and the vapor phase contains then a negligible portion of the total ^{3}He.

Motivated by Tisza [7, 8] and Landau's [9] two-fluid theory of superfluid ^{4}He, we can also consider dilute ^{3}He $-$ ^{4}He mixtures to be "two-fluid". One fluid is formed by superfluid ^{4}He, with exactly zero viscosity and entropy, while the other is formed by normal fluid ^{4}He, and ^{3}He "impurities". These two fluids can flow about each other without any viscous interaction.

If temperature were below 0.5 K, practically all ^{4}He would be in superfluid state, and the normal component would then be almost pure ^{3}He. At those temperatures, the mixture would behave like

Fermi-gas, since now the bosonic superfluid ^{4}He acts like an inert background that only affects the effective mass of ^{3}He. This system is interesting in its own right, as it is a Fermi system where we can alter the Fermi temperature by changing the ^{3}He concentration. Conversely, above the Fermi-temperature ($\sim 1\,\mathrm{K}$), ^{3}He behaves more like a classical gas.

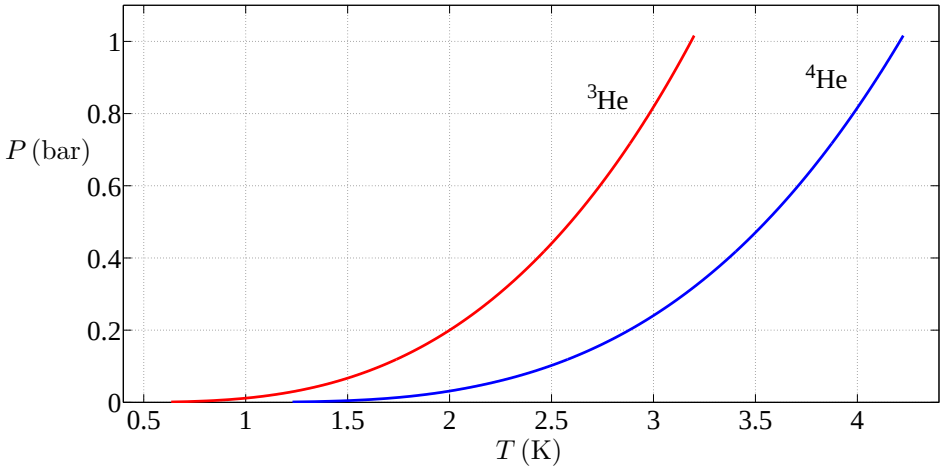

Figure 2.2: Saturated vapor pressure of ^{3}He (red) and ^{4}He (blue).

3 Sound Propagation in ^{3}He - Superfluid ^{4}He Mixtures

In this section, we set out to obtain expressions for the coupling factors between first and second sound in ^{3}He - superfluid ^{4}He mixtures. To do that, we must first find an expression for the sound velocities in the mixture.

In normal systems, temperature fluctuations are damped so much that they cannot propagate as temperature waves, but superfluid, on the other hand, can flow without dissipation up to some critical velocity. Due to the gap in the superfluid energy spectrum, excitations that enable the dissipation cannot be created below this critical velocity, and in freely flowing superfluid systems it is then possible to find propagating temperature waves, or second sound.

According to the two-fluid model, superfluid ^{4}He can be thought to consist of two components: superfluid and normal fluid. These two components can flow freely about each, meaning that at each point of the liquid there exist two independent velocity fields. In mixtures, it is further assumed that ^{3}He atoms move along with the normal fluid component, which has been proven accurate by Khalatnikov [10]. This assumption is valid when ^{3}He is in normal state, which is certainly true in the temperature region of our experiment. In terms of the two-fluid model, the first sound is a mode where the two components oscillate in phase, and a density (or pressure) wave is propagating through the system. In the second sound mode the superfluid component and the normal fluid component oscillate antiphase, and since only the normal component can carry entropy, this mode

is observed as an entropy (or temperature) wave. Additionally, since ^{3}He flows with the normal fluid component, the second sound can also be considered a ^{3}He concentration wave.

The total density of the ^{3}He - superfluid ^{4}He mixture is

$$\rho = \rho_{\mathrm{n}} + \rho_{\mathrm{s}}, \tag{3.1}$$

where ρ_{n} is the normal fluid density and ρ_{s} is the superfluid density. The normal fluid density consists of the normal component of ^{4}He ($\rho_{\mathrm{n},4}$) and ^{3}He component ($\rho_{\mathrm{n},3}$): $\rho_{\mathrm{n}} = \rho_{\mathrm{n},3} + \rho_{\mathrm{n},4}$. Since the motion of the superfluid component and the normal fluid component can be assumed to be independent, the total mass flux is

$$\mathbf{j} = \rho_{\mathrm{n}}\mathbf{v}_{\mathrm{n}} + \rho_{\mathrm{s}}\mathbf{v}_{\mathrm{s}}, \tag{3.2}$$

where $\mathbf{v}_{\mathrm{n}}$ and $\mathbf{v}_{\mathrm{s}}$ are the normal fluid velocity and superfluid velocity, respectively. Mathematically, the existence of second sound is a result of these two coexisting velocity fields.

The linearized two-fluid hydrodynamical equations are given by Khalatnikov [10]:

$$\frac{\partial \rho}{\partial t} + \nabla \cdot \mathbf{j} = 0 \tag{3.3}$$

$$\frac{\partial \mathbf{j}}{\partial t} + \nabla P = 0 \tag{3.4}$$

$$\frac{\partial (\rho\sigma)}{\partial t} + \rho\sigma \nabla \cdot \mathbf{v}_{\mathrm{n}} = 0 \tag{3.5}$$

$$\frac{\partial (\rho c)}{\partial t} + \rho c \nabla \cdot \mathbf{v}_{\mathrm{n}} = 0 \tag{3.6}$$

$$\frac{\partial \mathbf{v}_{\mathrm{s}}}{\partial t} + \nabla \left(\mu - \frac{Z}{\rho} c \right) = 0 \tag{3.7}$$

The first equation is the equation of mass conservation, and the second is due to the conservation of momentum (P is the pressure). The third equation is the conservation of entropy, where σ is the specific entropy (entropy per mass unit). The fourth equation is the continuity equation for the ^{3}He "impurities". Here c is the mass concentration of ^{3}He

$$c = \frac{m_3 N_3}{m_4 N_4 + m_3 N_3}, \tag{3.8}$$

where m_3 and m_4 are the atomic mass of ^{3}He and ^{4}He respectively, and N_3 and N_4 the number of ^{3}He and ^{4}He atoms, respectively. The mass concentration is related to the molar concentration x_3 through

$$c = \frac{x_3 m_3}{m_4 - x_3 (m_4 - m_3)}. \tag{3.9}$$

The fifth and final equation is the equation of motion of the superfluid component, where $\mu = c\mu_3 + (1 - c)\,\mu_4$ is the specific chemical potential with μ_3 and μ_4 being the chemical potentials

of the components of the mixture, and $Z \equiv \rho\,(\mu_3 - \mu_4)$. Using them we get an alternative form for eq. (3.7):

$$\frac{\partial \mathbf{v}_\mathrm{s}}{\partial t} + \nabla \mu_4 = 0, \tag{3.10}$$

telling us that the motion of the superfluid component is driven by the gradient in the chemical potential of ^{4}He.

3.1 Sound Velocity

Now we are ready to start working our way towards an expression for sound velocity in ^{3}He - superfluid ^{4}He mixture. The calculation presented here follows the same outline as the calculation carried out by Khalatnikov [10], and by Wilks [11] and Tilley [12] for pure ^{4}He, however we present it here in more detail.

We start by taking time derivative of eq. (3.3), and divergence of eq. (3.4) to obtain

$$\frac{\partial^2 \rho}{\partial t^2} = \nabla^2 P. \tag{3.11}$$

Next, we simply subtract eq. (3.6) from eq. (3.5) in order to get:

$$\frac{1}{\sigma}\frac{\partial \sigma}{\partial t} = \frac{1}{c}\frac{\partial c}{\partial t}. \tag{3.12}$$

To get the third equation, we first take time derivative of eq. (3.5) and divergence of eqs. (3.4) and (3.7), and eliminate the velocity terms to get

$$\rho_\mathrm{s}\nabla^2\left(\mu - \frac{Z}{\rho}c\right) - \nabla^2 P + \frac{\rho_\mathrm{n}}{\rho\sigma}\frac{\partial^2(\rho\sigma)}{\partial t^2} = 0. \tag{3.13}$$

Then, we eliminate the specific chemical potential μ by using the Maxwell relation

$$\mathrm{d}\mu = -\sigma \mathrm{d}T + \frac{\mathrm{d}P}{\rho} \;\Rightarrow\; \nabla^2\mu = -\sigma\nabla^2 T + \frac{\nabla^2 P}{\rho}, \tag{3.14}$$

where T is the temperature, to obtain

$$\frac{\rho_\mathrm{n}}{\rho_\mathrm{s}\sigma}\frac{\partial^2 \sigma}{\partial t^2} = \sigma\nabla^2 T + c\nabla^2\left(\frac{Z}{\rho}\right). \tag{3.15}$$

Eq. (3.11) is the first sound wave equation, and eq. (3.15) is the second sound wave equation.

We proceed by choosing T, P and c as our independent variables, and consider small perturbations around an equilibrium value, indicated by subscript 0, so that

$$\begin{aligned} T &= T_0 + \widetilde{T}\,(\mathbf{r},t) \\ P &= P_0 + \widetilde{P}\,(\mathbf{r},t) \\ c &= c_0 + \widetilde{c}\,(\mathbf{r},t)\,. \end{aligned} \tag{3.16}$$

Then, we can express the perturbations in ρ, σ, and Z/ρ using these three independent variables:

$$\begin{aligned} \widetilde{\rho} &= \left(\frac{\partial\rho}{\partial T}\right)_{P,c}\widetilde{T} + \left(\frac{\partial\rho}{\partial P}\right)_{T,c}\widetilde{P} + \left(\frac{\partial\rho}{\partial c}\right)_{T,P}\widetilde{c} \\ \widetilde{\sigma} &= \left(\frac{\partial\sigma}{\partial T}\right)_{P,c}\widetilde{T} + \left(\frac{\partial\sigma}{\partial P}\right)_{T,c}\widetilde{P} + \left(\frac{\partial\sigma}{\partial c}\right)_{T,P}\widetilde{c} \\ \widetilde{Z/\rho} &= \left(\frac{\partial\,(Z/\rho)}{\partial T}\right)_{P,c}\widetilde{T} + \left(\frac{\partial\,(Z/\rho)}{\partial P}\right)_{T,c}\widetilde{P} + \left(\frac{\partial\,(Z/\rho)}{\partial c}\right)_{T,P}\widetilde{c}. \end{aligned} \tag{3.17}$$

We further assume that all the variables have a plane wave form $\propto \exp\left(i\omega\left(\frac{z}{u}-t\right)\right)$, where ω is the angular frequency and u the velocity of the wave. We have chosen such a coordinate system that the perturbation propagates in the z-direction. When we insert these assumptions in the eqs. (3.11), (3.12), and (3.15), we obtain equations

$$\left(\frac{\partial\rho}{\partial T}\right)_{P,c}\widetilde{T} + \left(\frac{\partial\rho}{\partial P}\right)_{T,c}\widetilde{P} + \left(\frac{\partial\rho}{\partial c}\right)_{T,P}\widetilde{c} = \frac{\widetilde{P}}{u^2} \tag{3.18}$$

$$c_0\left(\frac{\partial\sigma}{\partial T}\right)_{P,c}\widetilde{T} + \frac{c_0}{\rho_0^2}\left(\frac{\partial\rho}{\partial T}\right)_{P,c}\widetilde{P} = \bar{\sigma}\widetilde{c} \tag{3.19}$$

$$\frac{u^2\rho_\mathrm{n}}{\rho_\mathrm{s}\sigma_0}\left[\left(\frac{\partial\sigma}{\partial T}\right)_{P,c}\widetilde{T} + \frac{1}{\rho_0^2}\left(\frac{\partial\rho}{\partial T}\right)_{P,c}\widetilde{P} + \left(\frac{\sigma_0-\bar{\sigma}}{c_0}\right)\widetilde{c}\right] = \bar{\sigma}\widetilde{T} - \frac{c_0}{\rho_0^2}\left(\frac{\partial\rho}{\partial c}\right)_{T,P}\widetilde{P} + c_0\left(\frac{\partial\,(Z/\rho)}{\partial c}\right)_{T,P}\widetilde{c}. \tag{3.20}$$

Where we have used the Maxwell relations [5]

$$\begin{aligned} \frac{\partial\,(Z/\rho)}{\partial P} &= -\frac{1}{\rho_0^2}\frac{\partial\rho}{\partial c} \\ \frac{\partial\,(Z/\rho)}{\partial T} &= -\frac{\partial\sigma}{\partial c} \\ \frac{\partial\sigma}{\partial P} &= \frac{1}{\rho_0^2}\frac{\partial\rho}{\partial T}, \end{aligned} \tag{3.21}$$

and, furthermore, we have defined $\bar{\sigma} \equiv \sigma_0 - c_0\frac{\partial\sigma}{\partial c}$.

When we next eliminate $\widetilde{c}$ from eqs. (3.18)-(3.20), we arrive to equations

$$u^2\left[\left(\frac{\partial\rho}{\partial T}\right)_{P,c}+\frac{c_0}{\bar{\sigma}}\left(\frac{\partial\rho}{\partial c}\right)_{T,P}\left(\frac{\partial\sigma}{\partial T}\right)_{P,c}\right]\widetilde{T}+$$

$$\left[u^2\left(\left(\frac{\partial\rho}{\partial P}\right)_{T,c}+\frac{c_0}{\bar{\sigma}\rho_0^2}\left(\frac{\partial\rho}{\partial T}\right)_{P,c}\left(\frac{\partial\rho}{\partial c}\right)_{T,P}\right)-1\right]\widetilde{P}=0, \tag{3.22}$$

and

$$\left[\frac{1}{\bar{\sigma}}\left(\frac{\partial\sigma}{\partial T}\right)_{P,c}U^2-\bar{\sigma}\right]\widetilde{T}+\left[\frac{1}{\rho_0^2\bar{\sigma}}\left(\frac{\partial\rho}{\partial T}\right)_{P,c}U^2+\frac{c_0}{\rho_0^2}\left(\frac{\partial\rho}{\partial c}\right)_{T,P}\right]\widetilde{P}=0, \tag{3.23}$$

where we have defined

$$U^2\equiv u^2\frac{\rho_\mathrm{n}}{\rho_\mathrm{s}}-c_0^2\frac{\partial\left(Z/\rho\right)}{\partial c}. \tag{3.24}$$

Now, (3.22) is the first sound wave equation, and (3.23) the second sound wave equation. Since the partial derivative $\left(\frac{\partial\rho}{\partial T}\right)_{P,c}=-\kappa\rho$, where κ is the thermal expansion coefficient, is very small for superfluid helium [10], we can ignore it to simplify our equations to

$$\left[u^2\frac{c_0}{\bar{\sigma}}\left(\frac{\partial\rho}{\partial c}\right)_{T,P}\left(\frac{\partial\sigma}{\partial T}\right)_{P,c}\right]\widetilde{T}+\left[u^2\left(\frac{\partial\rho}{\partial P}\right)_{T,c}-1\right]\widetilde{P}=0 \tag{3.25}$$

$$\left[\frac{1}{\bar{\sigma}}\left(\frac{\partial\sigma}{\partial T}\right)_{P,c}U^2-\bar{\sigma}\right]\widetilde{T}+\left[\frac{c_0}{\rho_0^2}\left(\frac{\partial\rho}{\partial c}\right)_{T,P}\right]\widetilde{P}=0. \tag{3.26}$$

As per usual, the system of equations (3.25) and (3.26) has a non-zero solution, if the determinant of its coefficients is zero, *i.e.*

$$u^4-u^2\left[\left(\frac{\partial P}{\partial\rho}\right)_{T,c}\left(1+\frac{\rho_\mathrm{s}}{\rho_\mathrm{n}}\left(\frac{c_0}{\rho_0}\left(\frac{\partial\rho}{\partial c}\right)_{T,P}\right)^2\right)+\frac{\rho_\mathrm{s}\bar{\sigma}^2}{\rho_\mathrm{n}}\left(\frac{\partial T}{\partial\sigma}\right)_{P,c}+\frac{\rho_\mathrm{s}c_0^2}{\rho_\mathrm{n}}\left(\frac{\partial\left(Z/\rho\right)}{\partial c}\right)_{T,P}\right]+$$

$$\frac{\rho_\mathrm{s}\bar{\sigma}^2}{\rho_\mathrm{n}}\left(\frac{\partial T}{\partial\sigma}\right)_{P,c}\left(\frac{\partial P}{\partial\rho}\right)_{T,c}+\frac{\rho_\mathrm{s}c_0^2}{\rho_\mathrm{n}}\left(\frac{\partial P}{\partial\rho}\right)_{T,c}\left(\frac{\partial\left(Z/\rho\right)}{\partial c}\right)_{T,P}=0. \tag{3.27}$$

This equation can be further simplified by noticing that $\left(1+\frac{\rho_\mathrm{s}}{\rho_\mathrm{n}}\left(\frac{c_0}{\rho_0}\left(\frac{\partial\rho}{\partial c}\right)_{T,P}\right)^2\right)\approx 1$, since $\frac{\rho_\mathrm{s}}{\rho_\mathrm{n}}\left(\frac{c_0}{\rho_0}\left(\frac{\partial\rho}{\partial c}\right)_{T,P}\right)^2\leq 0.012$ within our temperature and concentration range. Finally, we obtain two solutions for the sound velocity in ^{3}He - superfluid ^{4}He mixture

$$u_1^2=\left(\frac{\partial P}{\partial\rho}\right)_{T,c} \tag{3.28}$$

$$u_2^2=\frac{\rho_\mathrm{s}}{\rho_\mathrm{n}}\left(\bar{\sigma}^2\left(\frac{\partial T}{\partial\sigma}\right)_{P,c}+c_0^2\left(\frac{\partial\left(Z/\rho\right)}{\partial c}\right)_{T,P}\right), \tag{3.29}$$

where u_1 is the velocity of the first sound, of order 200 $\frac{\mathrm{m}}{\mathrm{s}}$, and u_2 the velocity of the second sound, roughly around 30 $\frac{\mathrm{m}}{\mathrm{s}}$.

In pure ^{4}He, the velocity of second sound reduces to $u_2^2 = \frac{\rho_\mathrm{s}}{\rho_\mathrm{n}}\sigma_0^2\left(\frac{\partial T}{\partial \sigma}\right)_P$, indicating that it is a temperature (or entropy) wave at a constant pressure. The term $c_0^2\left(\frac{\partial(z/\rho)}{\partial c}\right)_{T,P}$ is due to the addition of ^{3}He component. We can also see that the second sound can only exist in superfluid; if superfluid density ρ_s goes to zero, so does u_2. Conversely, first sound is a pressure wave at constant temperature.

We have to remember, however, starting from the linearized two-fluid hydrodynamical equations, our derivation has ignored all non-linear terms, and irreversible effects, as well as left out the effect of the thermal expansion, which resulted in the two sound modes being completely independent. In practice, both first and second sound are almost always present, as they are coupled together.

3.2 Sound Conversion and Coupling Factors

The coupling between first and second sound in pure ^{4}He is due to the thermal expansion, in helium mixtures there appears additionally a ^{3}He concentration dependent contribution. This means that first and second sound velocities, calculated in the previous section, cannot be true eigenvalues of the system since we had ignored the thermal expansion during their calculation. But, if we assume that the coupling between the sound modes is weak, they are good approximations of the true eigenvalues.

Since we have "forced" the eigenvalues of the system to be pure first sound and pure second sound, we can consider eqs. (3.22) and (3.23) independently. In fact, with these forced eigenvalues, they cannot be true at the same time, but we are simply going to ignore that contradiction by realizing that it is a result of our simplifications of the system. First, in order to gain information about the coupling between first and second sound, we excite first sound, and see how it converts into second sound, *i.e.* we insert the approximate eigenvalue u_1 into eq. (3.23), which was obtained from second sound wave equation (3.15). After a rearrangement we get

$$\widetilde{T} = \frac{U_1^2\left(\frac{\partial\rho}{\partial T}\right)_{P,c} + c_0\bar{\sigma}\left(\frac{\partial\rho}{\partial c}\right)_{T,P}}{\rho_0^2\bar{\sigma}^2 - \rho_0^2 U_1^2\left(\frac{\partial\sigma}{\partial T}\right)_{P,c}}\widetilde{P} = \beta\widetilde{P}, \tag{3.30}$$

where $U_1^2 \equiv u_1^2\frac{\rho_\mathrm{n}}{\rho_\mathrm{s}} - c_0^2\left(\frac{\partial(z/\rho)}{\partial c}\right)_{T,P}$. This equation represents the conversion of first sound into second sound. The coupling factor β determines the amplitude of the temperature oscillations accompanying the pressure oscillations in the plane wave. We can immediately see, had we omitted the $\left(\frac{\partial\rho}{\partial T}\right)_{P,c}$ term, this coupling factor would be zero in pure ^{4}He.

Then, similarly, to get the coupling between second and first sound, we insert u_2 into eq. (3.22) (first sound wave equation) to obtain

$$\widetilde{P} = -\frac{u_2^2\left[\left(\frac{\partial\rho}{\partial T}\right)_{P,c} + \frac{c_0}{\bar{\sigma}}\left(\frac{\partial\rho}{\partial c}\right)_{T,P}\left(\frac{\partial\sigma}{\partial T}\right)_{P,c}\right]}{u_2^2\left[\left(\frac{\partial\rho}{\partial P}\right)_{T,c} + \frac{c_0}{\bar{\sigma}\rho_0^2}\left(\frac{\partial\rho}{\partial T}\right)_{P,c}\left(\frac{\partial\rho}{\partial c}\right)_{T,P}\right] - 1}\widetilde{T}, \tag{3.31}$$

which can be simplified by noticing that, in the denominator, $\frac{c_0}{\bar{\sigma}\rho^2}\left(\frac{\partial\rho}{\partial T}\right)_{P,c}\left(\frac{\partial\rho}{\partial c}\right)_{T,P} \backsim 10^{-6}$ is small compared to $\left(\frac{\partial\rho}{\partial P}\right)_{T,c} \sim 10^{-3}$, giving us

$$\widetilde{P} = \left[\left(\frac{\partial\rho}{\partial T}\right)_{P,c} + \frac{c_0}{\bar{\sigma}}\left(\frac{\partial\rho}{\partial c}\right)_{T,P}\left(\frac{\partial\sigma}{\partial T}\right)_{P,c}\right]\frac{u_1^2u_2^2}{u_1^2 - u_2^2}\widetilde{T} = \alpha\widetilde{T}. \tag{3.32}$$

This is the conversion of second sound into first sound, with the coupling factor α determining the amplitude of pressure oscillations that accompany temperature oscillations. We note that in pure ^{4}He the coupling is quite weak due to the small $\left(\frac{\partial\rho}{\partial T}\right)_{P,c} = -\kappa\rho$ term. In superfluid helium, the thermal expansion coefficient, κ, is negative, which makes the first term in brackets of eq. (3.32) positive. The second term is due to added ^{3}He, and in it $\frac{c_0}{\bar{\sigma}} > 0$, and $\left(\frac{\partial\sigma}{\partial T}\right)_{P,c} > 0$, but $\left(\frac{\partial\rho}{\partial c}\right)_{T,P} < 0$, meaning that the second term is negative. It is then possible that at some conditions the two terms cancel out each other, decoupling first sound from second sound. At those specific conditions, second sound cannot create first sound, *i.e.* temperature oscillations occur without change in the density of the liquid. The goal of our experiment was to observe that particular phenomenon. As the ^{3}He concentration increases, the second term in brackets starts to dominate the coupling factor α, and the strength of the coupling starts to increase.

The coupling factors presented here are of similar form as the ones given by Brusov *et al.* [4]. However, they made a sign error in the bracketed term of eq. (3.32), as noted by Rysti [5], which prevented them from noticing that, at certain concentrations and temperatures, this coupling factor can indeed become zero.

Next, we discuss a little about double sound conversion, which becomes very important later, when we want to understand what is really happening in our experimental setup. Double sound conversion occurs either, when first sound is initially converted into second sound and after that back into first sound, or, alternatively, when second sound is turned into first sound and back. In both cases, the amplitude of the twice converted sound $\widetilde{P}'$ (or alternatively $\widetilde{T}'$) is proportional to the product of the coupling factors

$$\begin{cases} \widetilde{P}' = \alpha\widetilde{T} = \alpha\beta\widetilde{P} \\ \widetilde{T}' = \beta\widetilde{P} = \alpha\beta\widetilde{T}. \end{cases} \tag{3.33}$$

The calculations presented here, and in the previous sections, consider only pure first and second

sound modes, $\widetilde{P}$ and $\widetilde{T}$, respectively. In practice, we cannot create completely pure first sound, pressure oscillations at exactly constant temperature, but an oscillator that creates mainly first sound inevitably heats the medium it is immersed. We should then present this calculation in a sound mode basis that does not consist of pure first and second sound, but rather some superpositions of the two, where the first mode is mainly density oscillations with some small temperature oscillations, and the second other way around. However, we can construct an approximation of this situation using the concept of pure sound modes. We can say that the sound mode, $\widetilde{s}_0$, that our oscillator creates is pure first sound plus some pure second sound

$$\widetilde{s}_0 \sim \widetilde{P} + \widetilde{T}. \tag{3.34}$$

Pure first sound can generate pure second sound, and vice versa, which means that after single sound conversion (SSC) the total sound is

$$\widetilde{s}_{\mathrm{SSC}} \sim \widetilde{s}_0 + \beta\widetilde{P} + \alpha\widetilde{T}, \tag{3.35}$$

and after double sound conversion

$$\widetilde{s}_{\mathrm{DSC}} \sim \widetilde{s}_{\mathrm{SSC}} + \alpha\beta\widetilde{P} + \alpha\beta\widetilde{T} = \left(\widetilde{P} + \alpha\widetilde{T} + \alpha\beta\widetilde{P}\right) + \left(\widetilde{T} + \beta\widetilde{P} + \alpha\beta\widetilde{T}\right), \tag{3.36}$$

where the terms are arranged so that the first parenthetical term consists of pressure oscillations, and the second of temperature oscillations. Key thing is, whether we consider pure sound modes, or superposition modes, if the coupling factor α goes to zero, so do all the first sound modes generated in sound conversions.

3.3 Calculation of Sound Velocities and Coupling Factors

In order to determine the value of the coupling factors and the sound velocities, we must find expressions for the multitude of derivative terms present in the equations (3.28), (3.29), (3.30), and (3.32).

The derivatives of the specific entropy σ can be obtained by assuming that ^{3}He and ^{4}He form an ideal solution, meaning that the isotopes do not interact with each other. The specific entropy σ can then be written as [10, 11]

$$\sigma = (1-c)\,\sigma_{40} + c\sigma_{30} - \frac{R}{M_4}(1-c)\ln(1-x_3) - \frac{R}{M_3}c\ln x_3, \tag{3.37}$$

where σ_{40}, M_4 σ_{30}, and M_3 are the specific entropy and molar mass of pure ^{4}He and pure ^{3}He, respectively, and R is the molar gas constant. Hence, we get

$$\frac{\partial\sigma}{\partial T} = (1-c)\left(\frac{\partial\sigma_{40}}{\partial T}\right) + c\left(\frac{\partial\sigma_{30}}{\partial T}\right), \tag{3.38}$$

$$\bar{\sigma} = \sigma_{40} - \frac{R}{M_4} \ln(1 - x_3), \tag{3.39}$$

$$\frac{\partial \sigma}{\partial c} = \frac{\sigma - \bar{\sigma}}{c}, \tag{3.40}$$

and

$$c^2 \frac{\partial (Z/\rho)}{\partial c} = \frac{RTx_3}{M_4}. \tag{3.41}$$

The specific entropy values of pure ^{3}He were taken from Roberts *et al.* [13], and the specific entropy of pure ^{4}He from Kramers *et al.* [14], and Hill and Lounasmaa [15].

The total density of the helium mixture consists of superfluid ^{4}He, normal fluid ^{4}He, and ^{3}He, which is always at normal state in our temperature range. The contribution of ^{3}He to the normal fluid density, $\rho_{\mathrm{n},3}$, is [10, 11]

$$\rho_{\mathrm{n},3} = \rho \frac{m_3^*}{m_4} x_3, \tag{3.42}$$

where m_3^* is the effective mass of ^{3}He atom in the ^{3}He - superfluid ^{4}He mixture. For m_3^* we use a phenomenological formula

$$m_3^* = \left(1 - 0.57 \frac{n_4}{n_4^0}\right)^{-1} m_3, \tag{3.43}$$

from Baym and Pethick [16], where n_4 is the number density of ^{4}He, and n_4^0 is the number density of ^{4}He at $T = P = 0$. The value for n_4^0 was obtained from Manninen [17]. The normal fluid density contribution of ^{4}He, $\rho_{\mathrm{n},4}$, can be approximated by [5]

$$\rho_{\mathrm{n},4} = \rho (1 - c) \xi, \tag{3.44}$$

where ξ is the normal fluid fraction of pure ^{4}He, obtained from Donnelly and Barenghi [18]. We have to note, however, that using these approximations it is possible for the total normal fluid density to exceed the total density of the mixture when $\xi \approx 1$. We had to handle this by scaling the normal fluid densities for each concentration with its maximum value, so that the normal fluid fraction at T_λ is always exactly 1, as otherwise our model would not behave correctly near T_λ.

The derivatives of the total density of the mixture, ρ, can be obtained by first writing the density in terms of the molar volume of the ^{3}He - ^{4}He mixture, V_{m}:

$$\rho = \frac{M}{V_{\mathrm{m}}}, \tag{3.45}$$

where $M = x_3 M_3 + (1 - x_3) M_4$ is the molar mass of the mixture. According to Dobbs [19], in our temperature region, and at low ^{3}He concentrations, the molar volume can be expressed as

$$V_{\mathrm{m}} = V_{\mathrm{m},4} (1 + \eta x_3), \tag{3.46}$$

where $V_{\mathrm{m},4}$ is the molar volume of pure ^{4}He, and $\eta = (0.284 \pm 0.005) - \left[(0.032 \pm 0.003) \frac{T}{\mathrm{K}}\right]$ is an

experimentally determined parameter. Then, we find

$$\frac{\partial \rho}{\partial c} = \frac{M_3}{M_4}\left(\frac{x_3}{c}\right)^2 \frac{M_3 - (1+\eta)\, M_4}{\frac{M_4}{\rho_4}\left(1+\eta x_3\right)^2}, \tag{3.47}$$

and

$$\frac{\partial \rho}{\partial T} = \frac{\left[x_3\left(M_3 - M_4\right) + M_4\right]\left[\frac{1}{\rho_4}\frac{\partial \rho_4}{\partial T}\left(1+\eta x_3\right) + x_3 \frac{\partial \eta}{\partial T}\right]}{\frac{M_4}{\rho_4}\left(1+\eta x_3\right)^2}, \tag{3.48}$$

where we have expressed the molar volume of pure ^{4}He using the density of pure ^{4}He, ρ_4. Niemela and Donnelly [20] give an experimental formula for ρ_4, which is a function of $|T - T_\lambda\left(\text{pure } ^4\text{He}\right)|$, and using it as it is means that eqs. (3.47) and (3.48) do not take into account that the λ-point of the mixture changes with ^{3}He concentration. We resolved this by replacing T_λ in Niemela and Donnelly's formula with ^{3}He concentration dependent $T_\lambda\left(x_3\right)$, so that $\rho_4 \propto |T - T_\lambda\left(x_3\right)|$. This modification keeps the overall functional shape of ρ_4 intact, but it moves the curve in temperature so that the total density of the mixture ρ starts to increase more rapidly when approaching the λ-point, even at ^{3}He concentrations other than 0. The values for $T_\lambda\left(x_3\right)$ were determined from our experiment.

Fig. (3.1) shows the second sound velocity obtained from our calculations, while the different points indicate experimental second sound velocity values, for comparison. At very low ^{3}He concentrations there is a local maximum in the velocity at about 1.8 K, which subsequently disappears as the concentration is increased. The velocity curves end at the λ-point of the $^3\text{He} - ^4\text{He}$ mixture, where the second sound ceases to exist.

The rest of the experimental data collected from various sources [21], are shown in fig. (3.2), which also shows the behavior of the second sound velocity at temperatures below 1 K. Our model is in quite a good agreement with the experimental data down to temperature 1.3 K. We cannot compare the two below this temperature, as the experimental data that we used in our calculations end at there. Furthermore, at higher ^{3}He concentrations the discrepancy between our calculated model and measured data seems to increase, which is likely caused by the assumptions we made in calculating the molar volume, and density of the liquid, which limited the validity of our model to low concentrations.

Then, in fig. (3.3) the second sound velocity is shown as a function of the temperature relative to the λ-point temperature, the temperature scale that our experimental data is presented. Now, as the temperatures are scaled with T_λ, all the curves end at the same point.

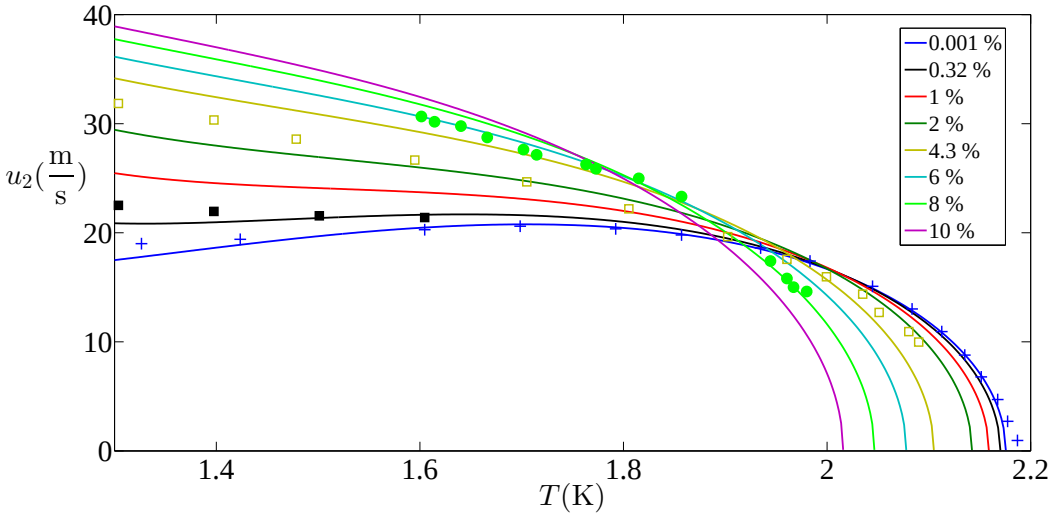

Figure 3.1: Velocity of second sound as a function of temperature, at ^{3}He concentrations between 0.001 % and 10 %. The various points indicate experimental second sound velocity data, read from fig. (3.2), in pure ^{4}He (+) [22–24], and in mixtures with ^{3}He concentrations 0.32 % (■), and 4.3 % (□) [25], and 8 % (•) [21]. The velocity has a local maximum in pure ^{4}He, at around 1.8 K, which subsequently disappears when the ^{3}He concentration is increased. At λ-point, the second sound velocity goes to zero.

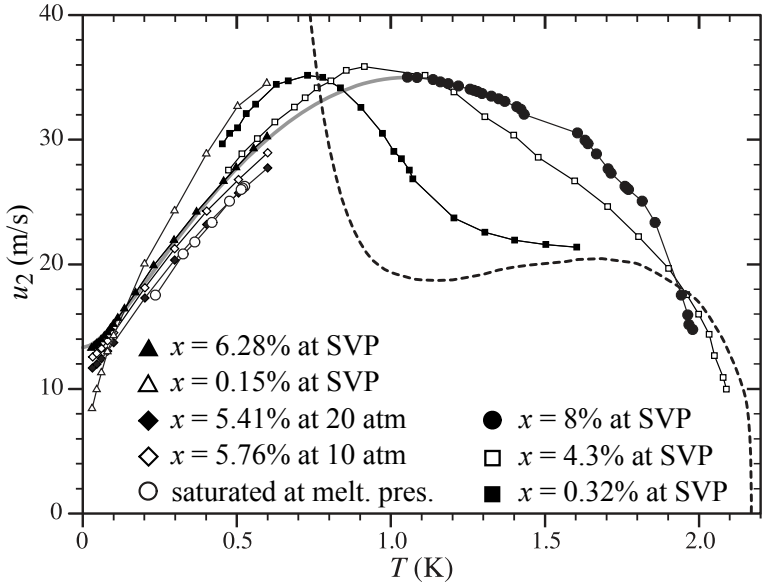

Figure 3.2: Experimental data for the second sound velocity in ^{3}He – ^{4}He mixtures. The dashed line is for pure ^{4}He at saturated vapor pressure [22–24], and other points are at different ^{3}He concentrations; 0.32 % and 4.3 % [25], and 0.15 %, 6.28 %, 5.41 %, and 5.76 % [26], and 8 % [21]. In mixtures, there is a maximum in the second sound velocity around 1 K.

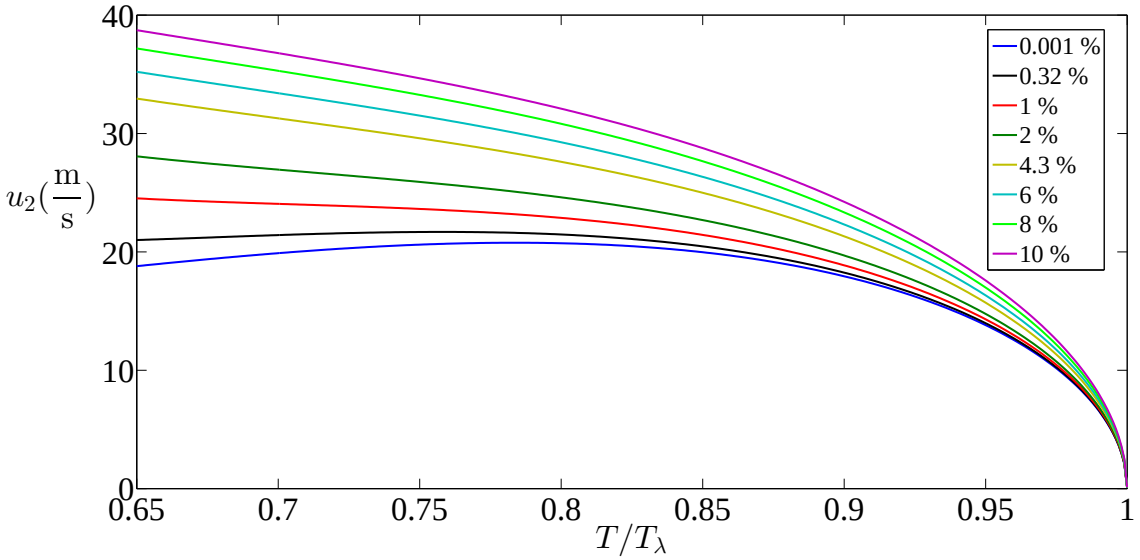

Figure 3.3: The velocity of second sound as a function of temperature relative to the λ-point temperature, at ^{3}He concentrations from 0.001 % to 10 %.

Next, we move on to the coupling factors. In order to obtain a value for them, besides the derivative terms described above, we need to know the first sound velocity u_1, which was obtained from Donnelly and Barenghi [18] for pure ^{4}He, and from Roberts and Sydoriak [27] for $^3\mathrm{He} - {}^4\mathrm{He}$ mixtures.

We first study separately the bracketed term of eq. (3.32), denoted $\widetilde{\alpha}$, in fig. (3.4). This is the term that determines when the two sound modes become decoupled, since from fig. (3.6) we see that the velocity factor in α is never smaller than zero, and zero only at T_λ. In pure ^{4}He, $\widetilde{\alpha}$ seems to go to zero at some very low temperature. Then, at 0.32 % ^{3}He concentration, for example, the two terms of $\widetilde{\alpha}$ cancel out each other at about $0.77T_\lambda \approx 1.7\,\mathrm{K}$, and as the concentration increases the decoupling temperature also increases, until after about 4 % concentration it no longer occurs. The $\widetilde{\alpha} = \alpha = 0$ line is shown in fig. (3.5).

On the other hand, first sound can always create second sound, as the coupling factor β , shown in fig. (3.6), is always non-zero. The product $\alpha\beta$ which represents the double sound conversion, shown at the bottom plot of fig. (3.6), naturally also disappears when $\widetilde{\alpha}$ goes to zero.

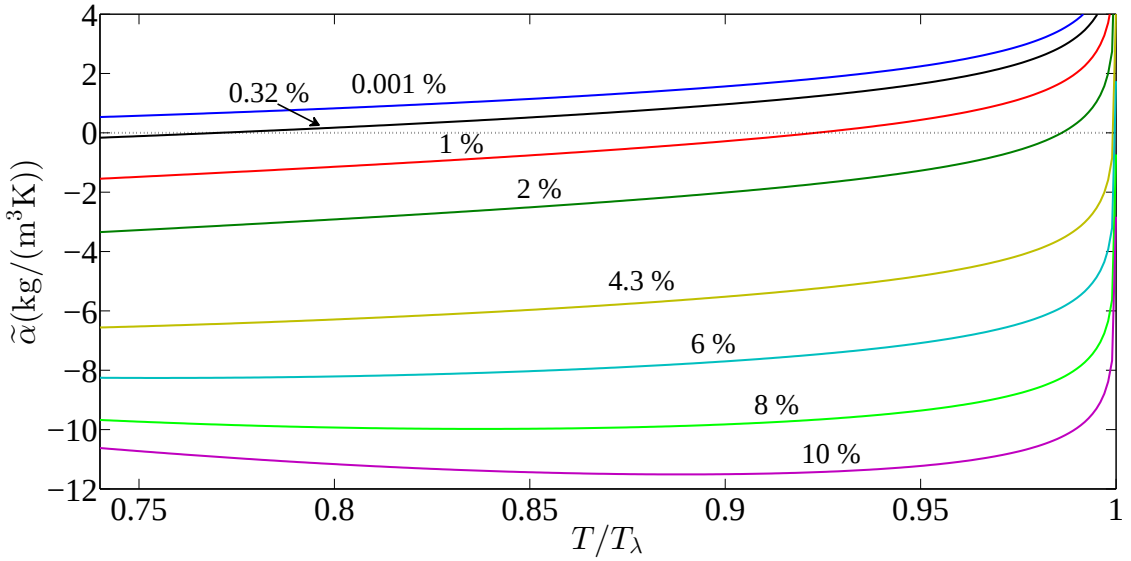

Figure 3.4: The bracketed term of eq. (3.32), $\widetilde{\alpha} = \left(\frac{\partial \rho}{\partial T}\right)_{P,c} + \frac{c_0}{\bar{\sigma}} \left(\frac{\partial \rho}{\partial c}\right)_{T,P} \left(\frac{\partial \sigma}{\partial T}\right)_{P,c}$, as a function of the temperature relative to the λ-point temperature, at ^{3}He concentrations between 0.001 % and 10 %. This term can go to zero at temperatures shown in fig. (3.5).

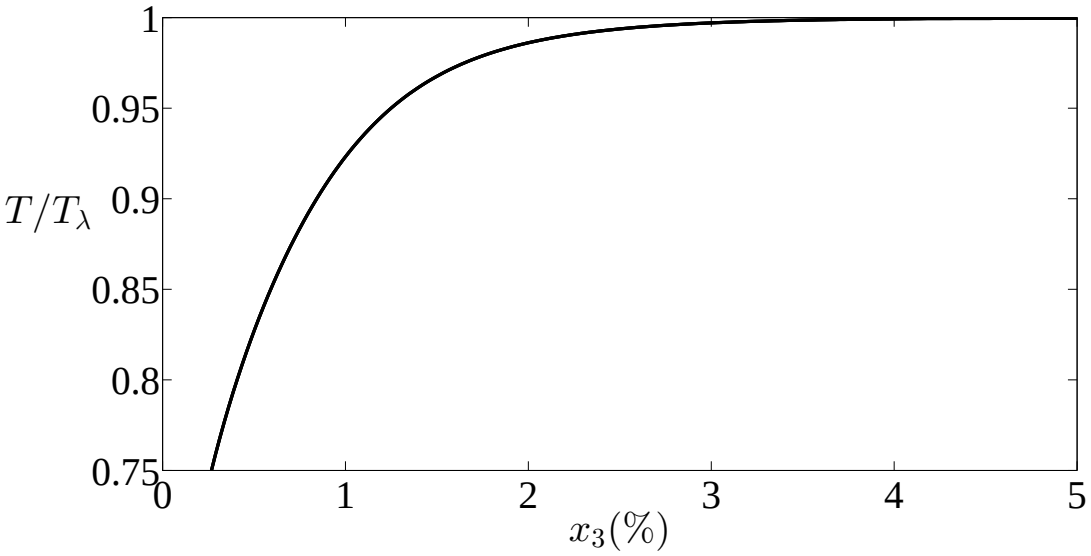

Figure 3.5: Decoupling temperature, temperature where $\alpha = 0$, as a function of ^{3}He concentration.

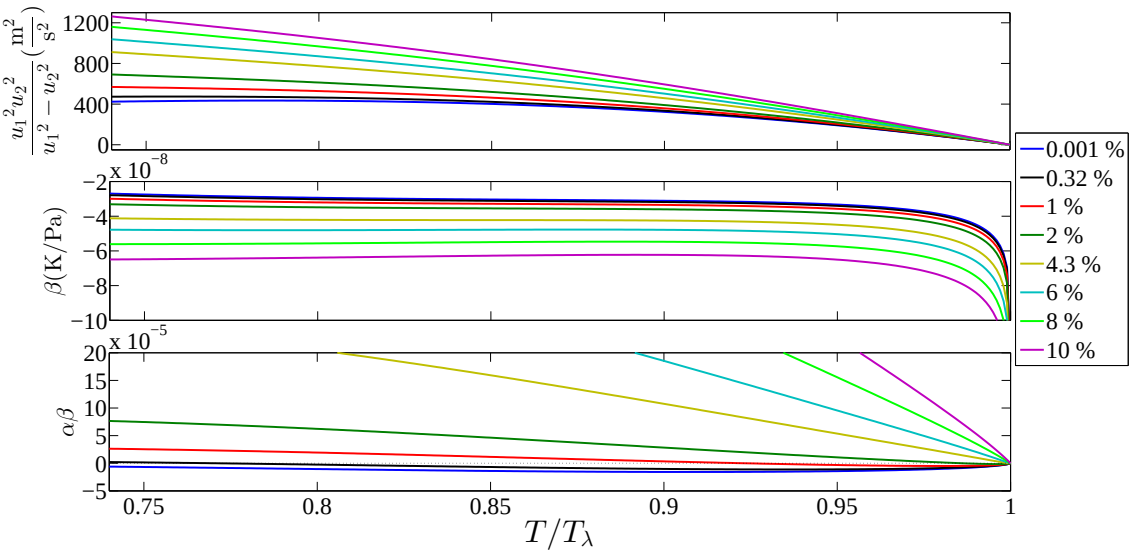

Figure 3.6: The velocity factor of α (eq. (3.32)), β (eq. (3.30)), and $\alpha\beta$ as a function of T/T_λ, at ^{3}He concentrations between 0.001 % and 10 %. The velocity factor and β do not change sign below the λ-point.

Since the coupling factor β is always non-zero, pressure oscillations are always accompanied by temperature oscillations, meaning, we cannot have on oscillating body in the liquid helium that does not cause some periodic heating and cooling of the medium. But this is not always case the other way around: there exists certain temperature and concentration values, where small periodic heating of the ^{3}He - ^{4}He mixture does not cause changes in the total density of the liquid. This decoupling behavior is the main focus of our experiment.

4 Quartz Tuning Fork Resonator

The main instrument in our experiment was a quartz tuning fork oscillator, which was used to directly observe the properties of $^3\mathrm{He} - {}^4\mathrm{He}$ mixture at different concentrations and temperatures.

Quartz tuning forks are commercially produced piezoelectric oscillators that are commonly used as frequency standards in various devices, such as watches. A properly cut and shaped quartz crystal can resonate at certain frequencies. These oscillators usually come in the shape of a traditional tuning fork, hence the name. There are number of possible resonant modes available, but the most commonly used is the one where the two tines oscillate antiphase toward each other with no nodes along the tines. The intended frequency for this mode is usually 2^{15} Hz $= 32768$ Hz at room temperature, although, the exact frequency changes slightly from fork to fork. The fork is excited by the metal electrodes placed on the surface of the tines.

Different kinds of mechanical resonators, ranging from wires to spheres, have long been used to

observe the properties of superfluid helium. When an oscillator is immersed in fluid, its response changes due to added inertia and dissipation of the medium, compared to vacuum environment. The quartz tuning forks, however, have several important advantages over the other oscillators. As they are mass produced, they are cheap and readily available, as well as robust and easy to install and use. Furthermore, unlike vibrating wires, they do not require magnetic field to operate, and are, in fact, insensitive to magnetic fields, which is a useful trait at many low temperature experiments. The main disadvantage of the forks is their rather non-trivial geometry making analytical calculations of their resonance behavior more difficult. Quartz tuning forks have been successfully used to measure, for example, temperature, pressure, viscosity, and turbulence in superfluid helium. [28]

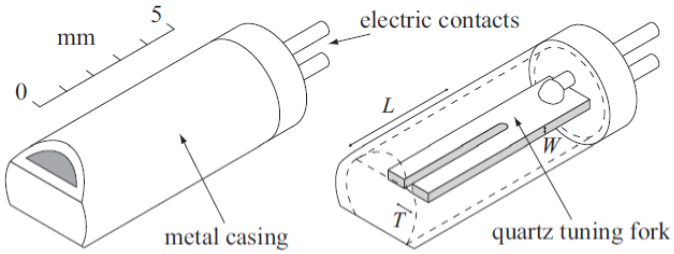

Figure 4.1: Schematic picture of a quartz tuning fork, with holes cut in its metallic container.

Quartz tuning forks come encapsulated in a hermetically sealed metallic container, often cylindrical in shape, as shown in fig. (4.1). The container has to either be completely removed, or have holes made in it to allow the fluid to reach the fork itself. The orientation of the fork within the container affects which resonant modes can be excited. This further adds to the uniqueness of the forks since no two forks have exactly the same position within their container. [5]

We used *ECS-.327-8-14X* 32.768 kHz, shown in fig. (4.2), and *ECS-.400-12.5-13* 40.000 kHz quartz tuning forks. However, the 40 kHz fork soon proved to be unreliable, of which more later, and the results presented in this thesis were obtained with the 32 kHz fork.

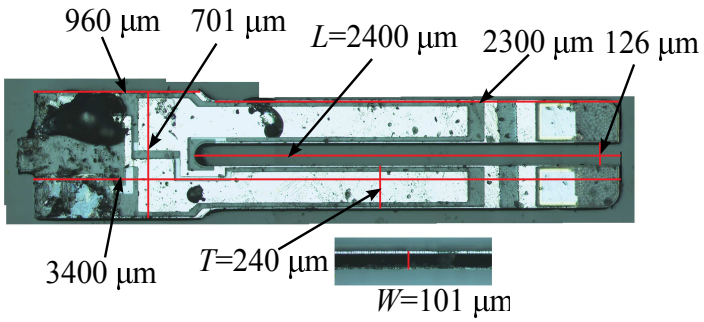

Figure 4.2: ECS-.327-8-14X, 32.768 kHz vacuum resonance frequency, quartz tuning fork with its dimensions.

In our setup (fig. (4.3)), we used a sinusoidal voltage from a function generator to excite the fork, and to apply a reference signal to a lock-in amplifier. The detection signal passes through a preamplifier before arriving to the lock-in amplifier. The two parameters that we want to measure from our fork are, of course, the resonance frequency, but also the width of the resonance, which is a very good indicator of the viscosity of the medium.

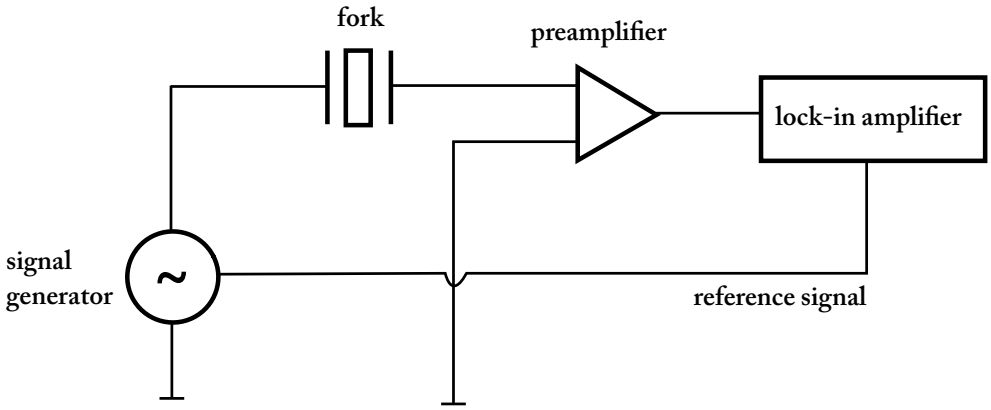

Figure 4.3: Circuit diagram of our quartz tuning fork measurement.

These two parameters were obtained using a resonance-tracking method, where we measure the fork signal at a single frequency close to the resonance frequency. When the resonator is operated in the linear regime, we can assume that the area of the resonance is frequency independent constant, and the shape of the resonance is a Lorentz function. This enables us to calculate the resonance frequency and resonance width based on a single measurement point. [21]

Before we can start to use the resonance-tracking method, we have to record a calibration spectrum over entire frequency range at stable conditions to determine the background offset and slope, the phase shift caused by the detection circuit, as well as the amplitude and width of the resonance peak. The main advantage of the resonance-tracking method is it being much faster than

recording entire spectra. Using the resonance-tracking method, it is possible to obtain a new data point every two seconds, whereas full frequency sweep would require minutes. The downside is that the full shape of the fork resonance is lost.

From our single frequency measurement, we get the two voltage components of the phase-corrected AC response, V_1 and V_2, which are related to the fork's resonance frequency, f_0, and resonance width, w, by [21]:

$$w = \frac{CV_1}{V_1^2 + V_2^2}, \tag{4.1}$$

and

$$f_0 = \sqrt{f\left(f + w\frac{V_2}{V_1}\right)}, \tag{4.2}$$

where the constant C is the product of the width and amplitude of the resonance peak, and f the measurement frequency.

For maximal accuracy, the resonance-tracking measurement would have to be done as close the fork's resonance frequency as possible, at least within the width of the resonance. To make this happen, we had a computer program which used the previous computed resonance frequency as the new measurement frequency. This algorithm meant that if the resonance frequency was changing too rapidly, the program could not follow it properly causing error in the computed resonance frequency. However, in our experiment the rate of change in temperature was so slow that the program had no difficulties in keeping track of the fork resonance.

As the data obtained from the resonance-tracking measurement are just the voltage data, we don't necessarily need to have exactly the correct resonance-tracking parameters in place during the measurement, rather, we can record them as a part of the measurement process and then apply them to the voltage data during the data analysis stage. The resonance-tracking parameters used in the measurements must, however, be good enough to enable the computer algorithm to properly track the resonance.

4.1 Second Sound Resonances in Quartz Tuning Fork

When a quartz tuning fork is oscillating in superfluid helium, it creates first sound as it pushes the liquid around it, but at the same time it also heats the liquid due to friction between the normal fluid component of helium and the surface of the fork. So, in practice, the oscillating fork creates a sound mode that is a combination of first and second sound.

In the temperature region of our experiment, the velocity of second sound is around $30\,\frac{\mathrm{m}}{\mathrm{s}}$, meaning that at the frequency region of 32 kHz the wavelength is of the order of a millimeter, which matches the scale of the quartz tuning fork and its container. The second sound created by the fork is then able to form a standing wave within the container of the fork. On the contrary, the velocity of first sound is roughly ten times larger than the velocity of second sound, meaning its wavelength is too long to form a standing wave around the fork. The second sound part of the sound mode

that the fork creates can then generate first sound, which can couple back to the fork altering its resonance response. A few possible standing wave modes within quartz tuning fork container are shown in fig. (4.4).

We discussed about these superposition sound modes at the end of Section 3.2, where, after double sound conversion, we ended up with the total sound wave

$$\widetilde{s}_{\mathrm{DSC}} \sim \left(\widetilde{P} + \alpha\widetilde{T} + \alpha\beta\widetilde{P}\right) + \left(\widetilde{T} + \beta\widetilde{P} + \alpha\beta\widetilde{T}\right). \tag{4.3}$$

Only the pressure oscillations of the first parenthetical term can alter the fork's resonance behavior, since the temperature oscillations of the second parenthetical term cannot create piezoelectric effect in the fork. The first pressure oscillation term $\widetilde{P}$ is first sound created by driving the fork and it has no significant temperature dependence, meaning it also cannot have an effect on the fork's resonance response. Conversely, $\alpha\widetilde{T}$ and $\alpha\beta\widetilde{P}$ have stronger temperature and concentration dependence due to the coupling factor α, and its effect can be observed. The coupling factor β has only a weak temperature and concentration dependence, which makes it difficult to determine which of the two first sound modes gained from sound conversions is dominant, or if either is.

On the other hand, we could simplify the situation by assuming that the fork creates only pure first sound. The pure first sound then can create pure second sound with coupling factor β. This second sound can then form the standing wave within the fork's container and again induce first sound, this time with coupling factor α. The entire process is then a double sound conversion, and the amplitude of the final pressure wave is proportional to the product of the coupling factors, $\alpha\beta$.

In our case, the important thing is that only the first sound modes can couple back to the fork, whereas second sound modes are invisible to the fork. Also, whether the first sound mode that couples back to the fork is a result from singe sound conversion ($\alpha\widetilde{T}$) or double sound conversion ($\alpha\beta\widetilde{P}$), it is still proportional to the coupling factor α. If it disappears, so does the coupling back to the fork, and that is exactly what we wanted to study.

When the coupling back to the fork occurs, the standing wave formed by the temperature wave drives a pressure wave at same wavelength, which can be detected by the fork. This can be seen as an anomaly in the resonance response of the fork, which appears as a loop in the fork's resonance frequency - resonance width graph. These anomalies, or these loops, are called *second sound resonances*, where the magnitude of the loop is directly proportional to the strength of the coupling between the two sound modes.

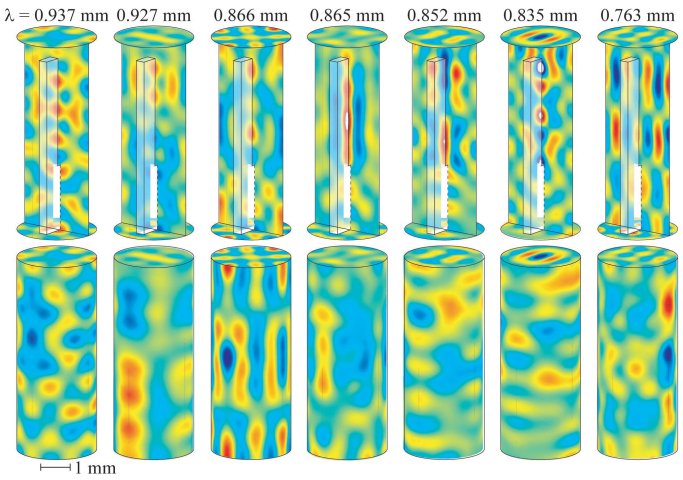

Figure 4.4: Some of the most strongly coupling standing wave modes in quartz tuning fork container with the oscillator placed symmetrically in the cavity. Blue and red colors indicate antinodes of the sound wave with opposing displacement from the equilibrium. The upper row shows sliced images, with the fork shown, and the lower shows the container surface. The wavelength of the sound wave is given above the image. [29]

5 Experimental Setup

The setup of our experiment consists of $^3\mathrm{He} - {}^4\mathrm{He}$ mixture cell placed in a $^4\mathrm{He}$ bath in a glass dewar. The mixture is monitored by the two quartz tuning forks discussed previously. The temperature of the bath is measured with two carbon resistors, and the bath and mixture cell pressure are measured with capacitive pressure gauges.

5.1 Mixture Cell

The mixture cell, presented in fig. (5.1), was made of copper, with stainless steel filling line on top, and with cupronickel and brass tubes on the side for the fork feedthroughs. The feedthroughs were made of different materials simply because we did not have a cupronickel tube with an appropriate diameter to fit the 40 kHz fork. The top section of the fork's container was completely removed to enable the $^3\mathrm{He} - {}^4\mathrm{He}$ mixture to reach the fork. The opened containers were then soldered to the tubes on the sides of the cell, and finally the tubes were wrapped in tissue paper, soaked with Stycast 1266 epoxy glue, to protect the fork feedthroughs from mechanical damage. At the bottom, there is a threaded hole for fastening the cell in place, however we did not end up using it.

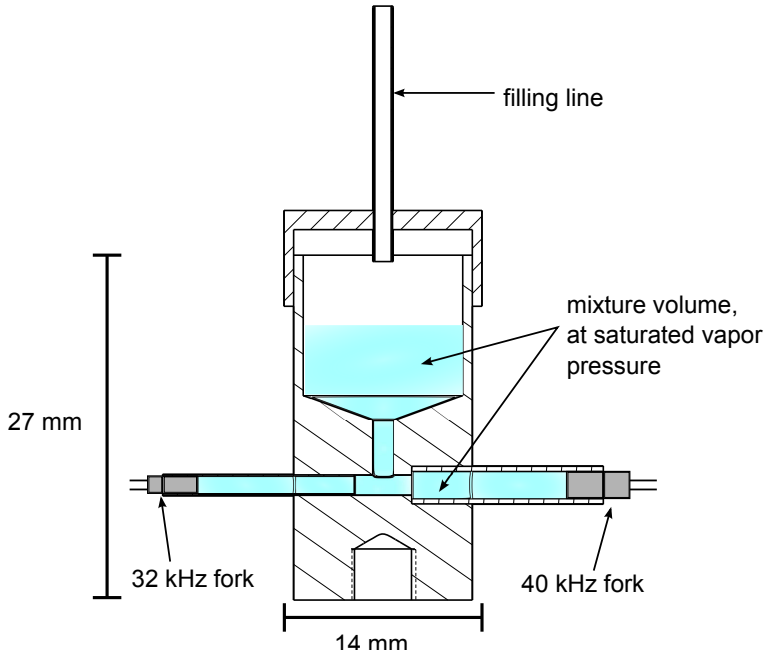

Figure 5.1: Schematic of the $^3\mathrm{He} - {}^4\mathrm{He}$ mixture cell. There is a buffer volume above the horizontal quartz tuning fork volume, which helps to keep the forks submerged and to maintain saturated vapor pressure in the mixture.

Strictly speaking, in order to observe second sound resonances, we would need just large enough volume of liquid to immerse the forks in it. However, we decided to include a larger buffer volume to help maintain the mixture at saturated vapor pressure, and to ensure that the forks remain properly submerged throughout our experiment. The total volume of the mixture cell was about $2\,\mathrm{cm}^3$, with the buffer volume making 94 % of it.

As the final step, we wrapped thin manganin wire, with total resistance of about $10\,\Omega$, around the cell as a heater.

5.2 Cooling System

The $^3\mathrm{He} - {}^4\mathrm{He}$ mixture cell was placed on a stand, as shown in fig. (5.2a), which could then be placed in a $^4\mathrm{He}$ bath in a glass dewar. Next, two Matsushita carbon resistor thermometers were installed, one ($50\,\Omega$) taped on top of the cell, and the other ($185\,\Omega$) a little higher, fixed on the support structure of the stand, to measure the temperature of the $^4\mathrm{He}$ bath. Additionally, we installed a $130\,\Omega$ power resistor heater on the bottom plate of the stand. A better view of the entire stand is in fig. (5.2b).

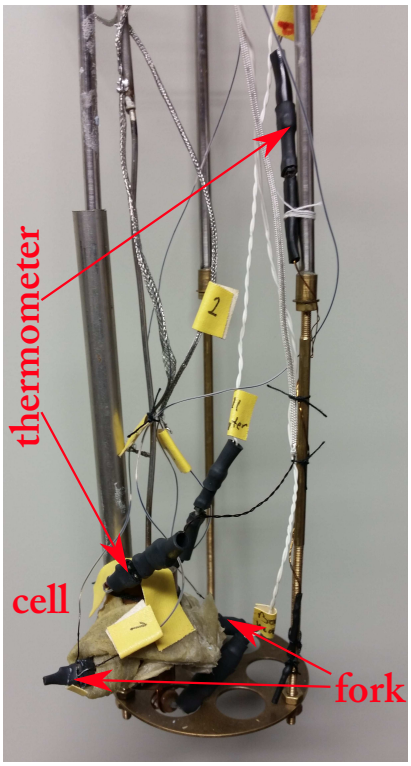

(a) Mixture cell installed on the stand of the glass dewar.

(b) Zoomed out view of the mixture cell on the stand.

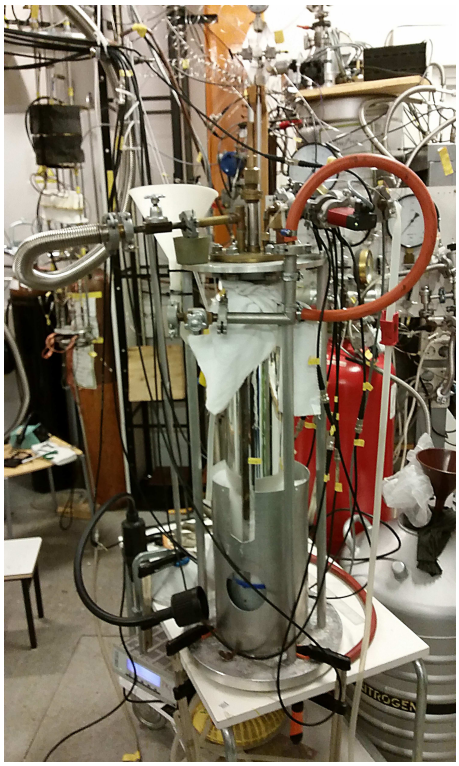

(c) Glass dewar during the experiment.

Figure 5.2

The glass dewar had a ^{4}He volume of about 2.5 liters, and smaller liquid nitrogen volume, separated by vacuum volume, for precooling and thermal shielding. The nitrogen volume was easily replenishable.

The ^{4}He bath was then pumped with a rotary pump to obtain temperatures down to 1.7 K. The cooling power is due to the latent heat of evaporation of liquid ^{4}He. When we pump away atoms from the vapor phase above the liquid, the most energetic atoms leave the liquid to replenish the vapor phase. Each atom transferred from liquid to vapor phase cools the liquid with the amount determined by the latent heat of evaporation. The cooling power decreases with temperature as $\propto \exp\left(-\frac{1}{T}\right)$, which imposes a limit to the lowest obtainable temperature, with small heat leaks and powerful pumps, to about 1 K for ^{4}He. [3]

As ^{4}He is pumped the liquid level in the bath decreases, this limits the time available at low temperature, since the ^{4}He bath cannot be replenished without warming it up to 4.2 K. The time available for our measurements was $7-8$ hours with full bath, which was just enough for a single measurement set. Initially, the liquid in the bath is consumed very rapidly, the cooling from 4.2 K at 1 bar to the λ-point at 2.18 K and 50.4 mbar expends roughly one quarter of the total amount of the liquid. After that, the consumption is significantly lower.

The pressure gauge of the ^{4}He bath was placed on the tube on the top flange of the glass dewar's stand, while the mixture cell pressure gauge was placed on the room temperature end of the filling line of the cell. Both pressure sensors were Pirani gauges with capacitive mode.

A photograph of the fully equipped glass dewar is in fig. (5.2c). The table where the class dewar stands is not protected from vibrations, but the buffer volume of the mixture cell makes it insensitive to external mechanical vibrations, and they then caused no problems.

A useful feature of the glass dewar is a "window", through which it is possible to actually see the liquid in the ^{4}He bath. This made it easy to monitor the liquid level of the bath, and to visually observe the bath's superfluid transition. In normal state, boiling liquid ^{4}He bubbles like any other boiling liquid. However, when the transition to the superfluid occurs the bubbling suddenly stops and the surface of the liquid is completely calm, even though it still is at a boiling point. This is due to the extremely large thermal conductivity of the superfluid ^{4}He, which means that the entire liquid is exactly at boiling temperature, as opposed to normal fluid, where only some points of the liquid are at boiling point.

6 Experiment Procedure

6.1 Room Temperature Preparations

The $^3\mathrm{He} - {}^4\mathrm{He}$ mixtures used in our experiment were prepared at room temperature. We started with commercial quality pure ^{4}He gas placed in a known volume, and then added $^3\mathrm{He} - {}^4\mathrm{He}$ mixtures of known concentrations of (6.0 ± 0.3) % and (11.0 ± 0.3) % to get mixtures with ^{3}He concentration ranging from 0 % to 9 % with about 0.5 percentage point interval. The amount of mixture to be added was calculated by assuming that the gaseous helium mixture was a mixture of two ideal gases. For two of the measurements, we used the gas directly from the known concentration tanks.

After each measurement, we gathered the mixture back with our gas handling system, and simply added some amount of richer mixture to it to make up the mixture for the next measurement. Initially, we had 25 mmol of pure ^{4}He, and finally ended up with 94 mmol of 9 % mixture. The amount interval was chosen so that at the beginning there would be enough liquid in the mixture cell to partly fill the buffer volume, and at the end we could still put all the mixture in the cell without risking it being completely full.

The ^{3}He concentration of the "known" concentration tanks was determined by a sound speed measurement at room temperature. Since ^{3}He is lighter than ^{4}He, increasing its concentration decreases the overall density of the mixture increasing the speed of sound. We had a chamber with known geometry, equipped with a speaker and a microphone placed at the antinodes of a certain standing sound wave forming inside the chamber. Then we made a frequency sweep to find the resonance frequency and compared it to the reference value of commercial quality pure ^{4}He, to determine the ^{3}He concentration. The chamber was placed in a water bath to keep it at a constant temperature, and in order to prevent contaminations in the helium gas from entering the chamber,

the gas went first through an activated charcoal trap at liquid nitrogen temperature (77 K) where the contaminants would freeze.

We learned that the pure ^{4}He reference value varied somewhat from day to day, which meant that the temperature inside the chamber was not kept perfectly constant. Also, the residual impurities left in the gas handling system could have caused some error. The ^{3}He concentration values were then obtained as an average value after measuring their concentrations on several days.

The volume of the sound speed measurement chamber plus the liquid nitrogen trap was so large that we could not use this setup to measure the concentration of the mixtures prepared for our mixture cell. To do so we would have had to prepare larger amounts of the mixture, and there was not enough room in our gas handling system to store it. However, the key thing for us was to prepare mixtures with steadily increasing concentrations, rather than to prepare mixtures with some specific concentrations. Eventually, we determined the concentrations of the prepared mixtures with the quartz tuning fork, using the (6.0 ± 0.3) % and (11.0 ± 0.3) % mixtures as calibration points.

6.2 Procedure at Low Temperatures

When the glass dewar was full of liquid ^{4}He at 4.2 K, we allowed the prepared $^3\text{He} - ^4\text{He}$ mixture to enter the mixture cell through the filling line. At the same time, we started to pump the ^{4}He bath to lower its temperature. ^{4}He has one degree higher boiling point than ^{3}He, meaning that, at first, mostly ^{4}He is condensing in the cell. Only below 3 K there starts to be significantly more ^{3}He in the liquid.

As soon as we reached the λ-point, we started our controlled temperature sweep. It was done by combination of adjusting the pumping of the ^{4}He bath with a valve, and heating the bath with a control loop feedback controlled heater. We tuned the pumping so that the temperature decreased a little too quickly, and then heated the bath just enough to slow it down to an appropriate level.

The controlled heater used a PID control loop, which allows us to give it a temperature sweep profile to follow, and the algorithm takes into account the current difference between the actual and the desired temperature (**P**roportional), and past difference based on the sum of earlier differences (**I**ntegral), as well as the anticipated difference based on current rate of change (**D**erivative). The current through the heating resistor is then adjusted according to this algorithm to produce the desired temperature sweep. Initially, our intention was to use the heater wire wrapped around the cell for the PID controller, but we learned that the power resistor placed at the bottom of the bath was more suited to the task, since with it we were able to obtain a steadier sweep rate.

Our temperature sweep profile was a linear with decrease rate of $0.5\,\frac{\text{mK}}{\text{min}}$ between the λ-point and about 2 K, and slightly faster, $1.5\,\frac{\text{mK}}{\text{min}}$, below 2 K. The temperature sweep back to the λ-point from the lowest temperature was done somewhat faster, as this way we were able to carry out all the measurements for a single concentration in the time window of 7-8 hours, which was determined by the amount of ^{4}He in the glass dewar. Moreover, we found that it was easier to maintain steady sweep rate while going down in temperature than going up.

The resistor thermometers were calibrated against saturated vapor pressure during the pure ^{4}He

runs. The vapor pressure was converted to temperature according to the *ITS-90* temperature scale. We found, that of the two installed carbon resistors, the one fixed on the support structure of the stand was slightly more sensitive to temperature changes, and we used it as our main thermometer. The second thermometer, taped directly on top of the mixture cell, was used as a backup. We made runs in pure ^{4}He both before and after the measurements in other ^{3}He concentrations to verify that our experimental setup had not changed in between.

All the while the temperature sweeps were going on, we were measuring the resonance frequency and resonance width of the two quartz tuning forks using the resonance-tracking method discussed in Section 4. During each cooldown, we stopped the temperature sweep at some point, and used the PID controller to maintain constant temperature to record a full quartz tuning fork spectrum in order to obtain new parameters for our resonance-tracking measurement.

7 Results

7.1 Second Sound Resonances

We begin by looking at the 32 kHz quartz tuning fork resonance data obtained during a single glass dewar cooldown period, with 4.2 % ^{3}He concentration mixture, which is presented in fig. (7.1). The superfluid transition shows clearly in the fork's resonance frequency - resonance width plot as a tilted V-shape near the 20 Hz resonance width. Below the λ-point, the resonance frequency of the fork increases with decreasing temperature, while above it is the other way around. The width of the fork's resonance decreases with decreasing temperature both above and below the λ-point, but below the change is more rapid.

When we are initially cooling down the mixture, far left in fig. (7.1), the superfluid transition curve starts to form in a different location than where it eventually ends up being. This is due to the two helium isotopes not properly mixing until the superfluid transition. As we cool down the helium mixture somewhat slowly from room temperature, mostly ^{4}He liquefies at first due to its higher boiling point, and then ^{3}He liquefies on top of it, and because it is lighter than ^{4}He, and because we are not disturbing the cell, it tends to stay there. When both isotopes are in normal state, their mixing due to diffusion is rather slow, and because the fork is at the bottom of the cell, mixture around it contains less ^{3}He than mixture closer to the surface. When ^{4}He becomes superfluid, it can flow without viscosity, driven strongly even by a small temperature gradient, which mixes the two isotopes very efficiently throughout the liquid volume. This feature can assist us in determining the location of the true λ-point, but we can only utilize it at concentrations above 2 %, for below it, this effect becomes quite small.

When the fork data are presented in the frequency-width plot, the second sound resonances are easily distinguishable, they appear as loops against the background slope that is caused by the temperature sweep. The magnitude of the loop is directly proportional to the coupling strength between first and second sound. Also, the sequence of the appearing resonances remains the same, even as we change the ^{3}He concentration; if there are two small resonances followed by a large

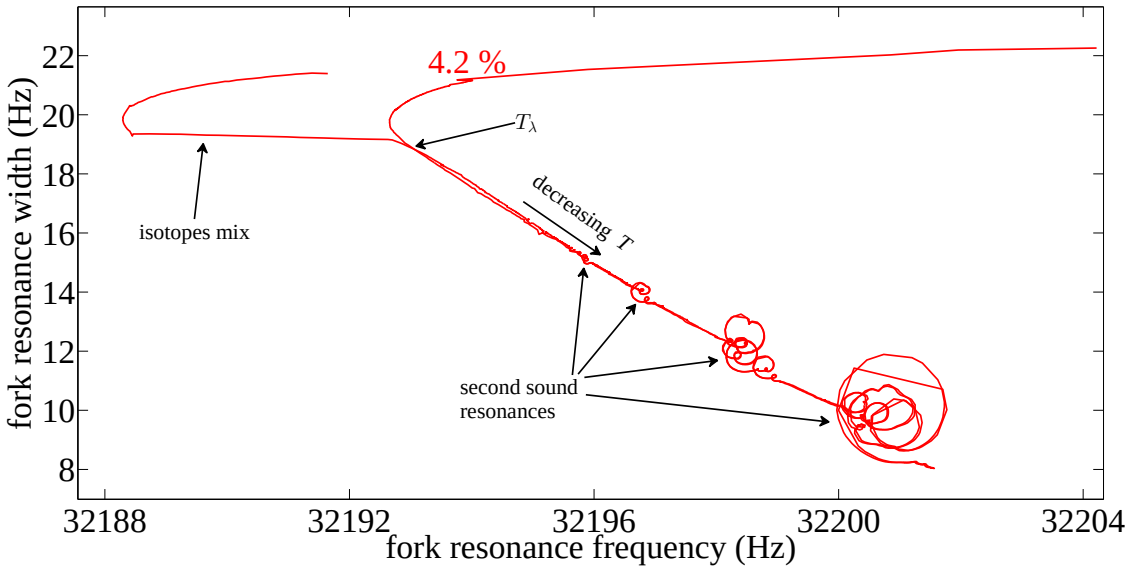

Figure 7.1: Fork resonance width versus fork resonance frequency in 4.2 % ^{3}He concentration mixture during the temperature sweep from about 2.6 K (slightly above T_λ) to 1.7 K and back, with key features indicated by the arrows.

one, or several small resonances within a large one, at one concentration, the same is true in other concentrations as well. This means, that even though the shape of the second sound resonances changes from concentration to concentration, it is possible to identify equivalent series of loops.

Alternatively, we can, for example, present the fork resonance width as a function of temperature, as in fig. (7.2), where we notice that the width of the second sound resonance in temperature increases with decreasing temperature. Near the λ-point, both the amplitude and width of the second sound resonances are small, making them very hard to distinguish, whereas at lower temperatures they clearly stand out. When the amplitude of the second sound resonance is large, this presentation works almost as well as the frequency-width plot. However, smaller resonances may be lost to the background noise, whereas they would still have distinct loop-like shape in frequency-width plot. Also, the region where the two isotopes mix is very difficult to discern in the temperature-width plot.

The rest of the quartz tuning fork resonance data obtained with the 32 kHz fork are shown in fig. (7.3). The temperature sweeps were carried out down to about 1.8 K in the first few measurement runs. Then, starting from 2.1 % mixture run, they were extended to about 1.7 K. Finally, the 11.0 % mixture run was again stopped at the higher temperature, as its main purpose was to calibrate our ^{3}He concentration scale. The temperature sweep rate of the 11.0 % run was also somewhat faster than in other measurements.

Below T_λ, the behavior of the background slope of the fork resonance frequency-width plot can be understood in terms of the two-fluid model: as temperature decreases the superfluid portion of

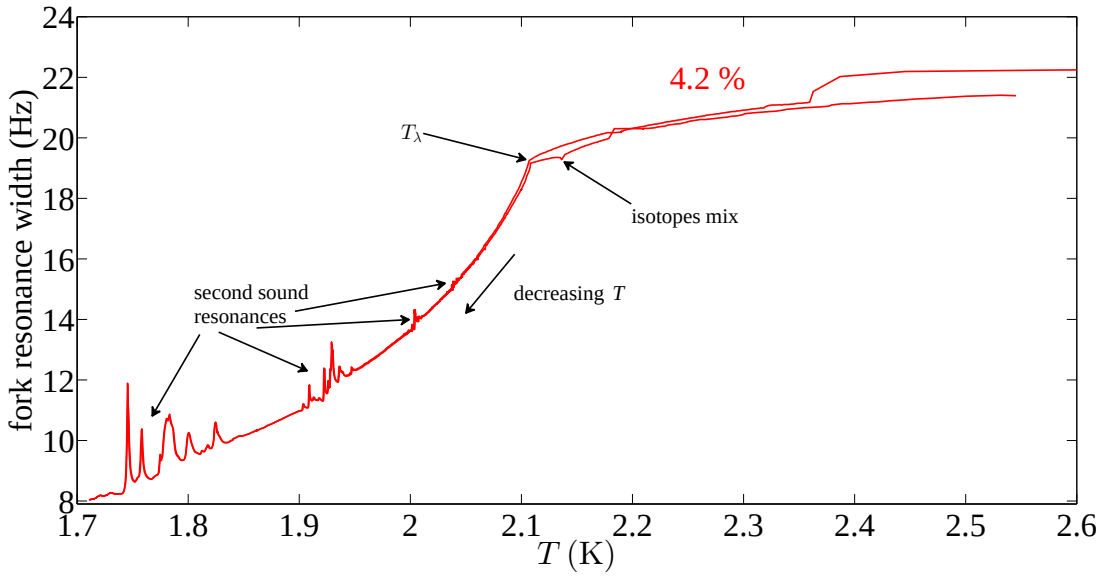

Figure 7.2: Fork resonance width versus temperature in 4.2 % ^{3}He concentration mixture during the temperature sweep. Same key features as in fig. (7.1) are highlighted.

the two-fluid increases, and since it has no viscosity that could dampen the fork's oscillations, we see a sharper resonance peak. On the other hand, as we increase the ^{3}He concentration, we are effectively increasing the normal fluid portion of our two-fluid, since in our temperature region ^{3}He cannot be in superfluid state. This means, that as we go towards higher concentrations, at constant temperature, the fork resonance width increases.

Since fig. (7.3) contains both the temperature sweep down and temperature sweep up, we can see that the second sound resonances of the 32 kHz fork appear, with good accuracy, at same location, independent of whether we were increasing or decreasing temperature. The same was not true for the 40 kHz fork. We measured the pure ^{4}He spectrum several times during the initial tests of our experimental setup, and already during this phase it became clear that the 40 kHz fork could not reproduce the locations of its second sound resonances within any sensible accuracy. Even during the same cooldown, the location of a single resonance seemed to shift arbitrarily. Since, during the same time, the 32 kHz fork worked well in comparison, we decided not to replace the 40 kHz fork, but rather went on with our experiment. We kept measuring the 40 kHz fork parallel with the other fork, but its poor behavior persisted throughout the experiment. All the data presented here were then obtained using the 32 kHz fork.

There were also some difficulties with the 32 kHz fork during the 1.1 % concentration experiment, as its curve is clearly shifted from the others. We could not identify any apparent reason for the shift, as the quartz tuning fork behaved otherwise just like before. Curiously, similar thing occurred during one of the pure ^{4}He measurements that were done after the other mixture runs, but it was remedied by thermal cycling our setup back to the room temperature. It is possible, that these shifts

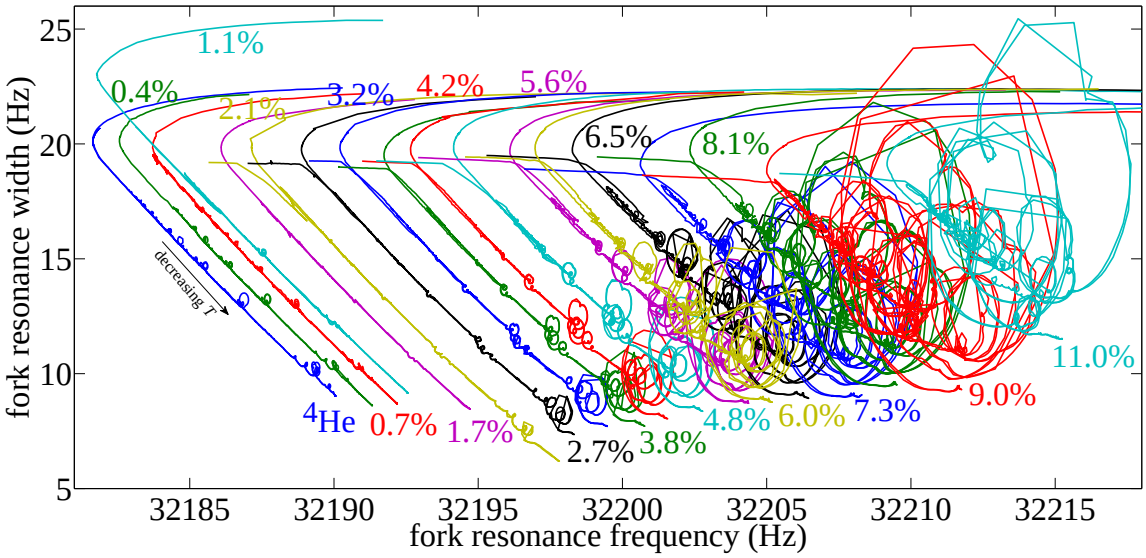

Figure 7.3: Resonance width of the 32 kHz quartz tuning fork versus the resonance frequency of the fork. Colors indicate different ^{3}He concentrations, which are given next to the curves. The background slope of the graphs is due to change in temperature, and the second sound resonances appear as loops. Note, that the 11.0 % dataset does not include the largest low temperature resonances.

are somehow related to small changes in the fork's measurement circuit, orientation of the wires, for example. We tried to keep the measurement circuit as unchanged as possible, but as there were other experiments running parallel with ours, some small variations were unavoidable. Then again, we recorded new tracking parameters for our resonance-tracking method during each cooldown, which should have mostly eliminated the error caused by the changes in the fork measurement circuit. It is also possible that some residual impurities in helium, like hydrogen, could have frozen on the surface of the fork changing its resonance response. This would explain why the problem did not occur in consecutive measurement runs, as the impurities would have evaporated away when we warmed up our setup to room temperature in between measurements.

Because of this shift, in 1.1 % concentration run, we started our temperature sweep at such low a temperature, that we missed the small resonances near T_λ. But, on the other hand, its temperature sweep was carried out to a lower temperature than in most of the previous measurements, which shows that the largest low temperature second sound resonances, that become very prominent at high concentrations, had not yet appeared at 1.1 % concentration.

The general region of the superfluid transition can easily be determined from the tilted V-shape clearly visible in all measurements in fig. (7.3). However, the exact location of the λ-point is slightly more challenging to determine. Guided by the fork response during the "isotopes mix" stage of fig. (7.1), we have placed the λ-point at the point, where the fork response curve starts to shift from the below T_λ background curve. The λ-points determined this way are presented in fig.

(7.4). The general behavior of T_λ is consistent with the data from Taconis and de Bruyn Ouboter [30], although our method gives systematically lower T_λ than their results. Since the data given by Taconis and de Bruyn Ouboter uses the outdated *ITS-48* temperature scale, we have scaled it linearly to match the current *ITS-90* temperature scale.

The λ-points were determined during the warm up stage of the experiment, and the temperature value was obtained from the carbon resistor thermometer. The location of the superfluid transition determined from the quartz tuning fork response may be correct, but at that instant the carbon resistor may not yet have warmed up to the exactly same temperature as the liquid surrounding it, giving us slightly too low T_λ value. Nevertheless, as we start to present our data in a temperature scale relative to the λ-point, the effect of the error in our T_λ should be reduced.

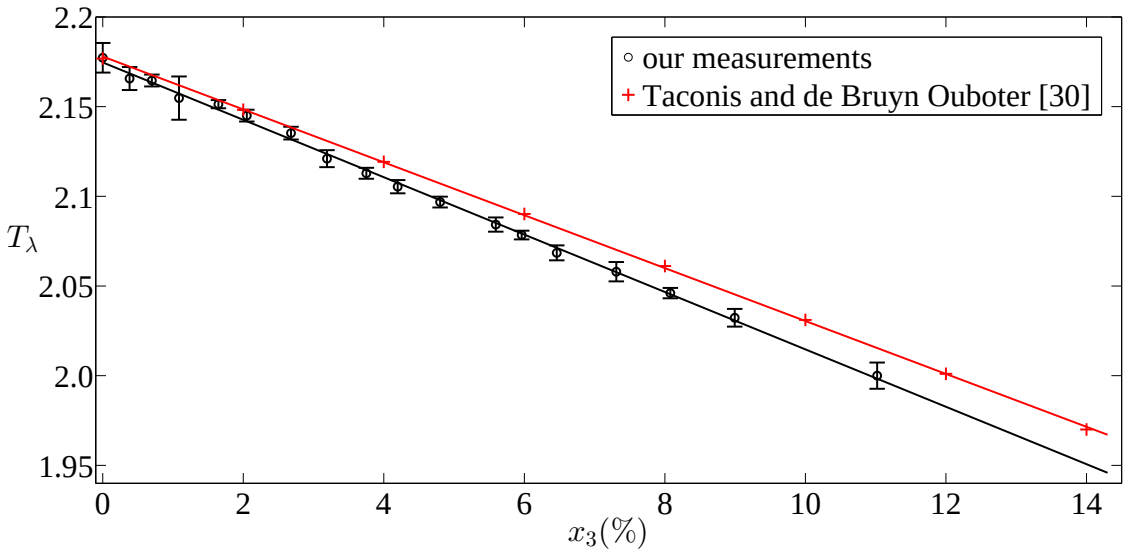

Figure 7.4: Superfluid transition temperature T_λ determined from our measurements (black), compared to the data from Taconis and de Bruyn Ouboter [30] (red).

The ^{3}He concentrations of fig. (7.3) were determined by making a linear fit to the background slope of each measurement set below T_λ. We chose the fork resonance frequency axis as our reference line, which means that the ^{3}He concentration is proportional to the ratio of the constant term and the slope of the linear fit. Since three datasets were obtained with known ^{3}He concentrations, one with pure ^{4}He, and the other two with (6.0 ± 0.3) % and (11.0 ± 0.3) % concentration mixtures taken directly from our room temperature storage tanks, we are able to determine the

concentrations of the rest of the mixtures. The linear fits are shown in fig. (7.5). The error of those concentrations was estimated to be ±0.3 percentage points, which is mostly due to the uncertainty of the storage tank mixture concentrations.

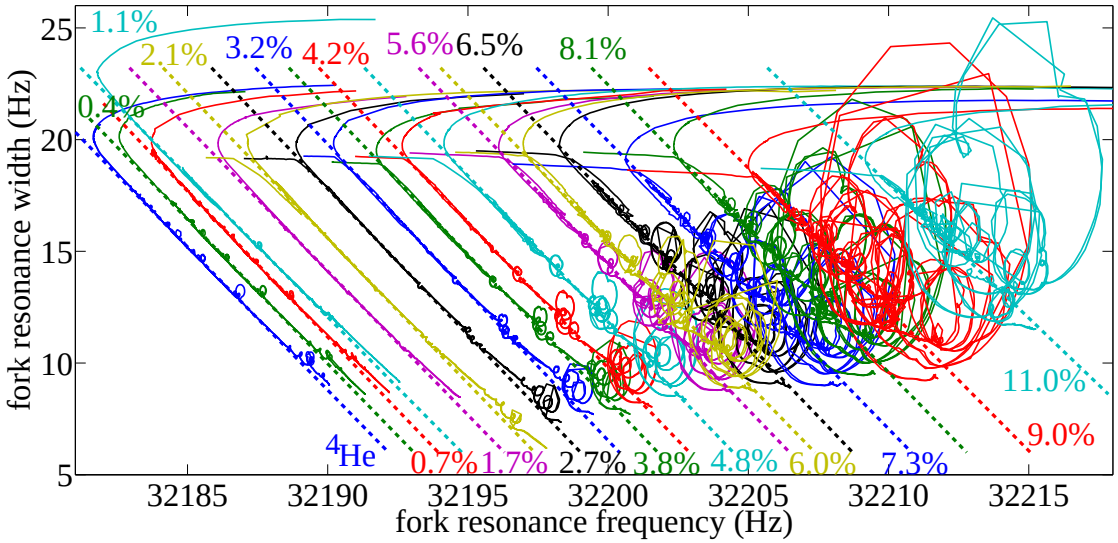

Figure 7.5: Linear fits to the background slopes of the fork data used to determine the ^{3}He concentrations.

The pure ^{4}He data presented in fig. (7.3) were obtained during one of the runs that were made after all the other mixture runs. For comparison, in fig. (7.6), we have two additional pure ^{4}He datasets obtained before any other mixture measurements. In one of them, the temperature sweep was extended to the lowest reachable temperature with our cooling system, 1.7 K. We see that the lowest temperature second sound resonances, that first appear at 2.1 % concentration in fig. (7.3), are absent in pure ^{4}He. Because we had not extended all the temperature sweeps at low ^{3}He concentrations so close to the minimum temperature, the dataset for the lowest temperature resonances is somewhat incomplete. Fortunately, since we had not noticed the shift of the problematic 1.1 % measurement set until afterward, we had carried out its temperature sweep down to almost 1.7 K. As these resonances had not yet appeared there, we can then narrow down the ^{3}He concentration they appear to somewhere between 1.1 % and 2.1 %.

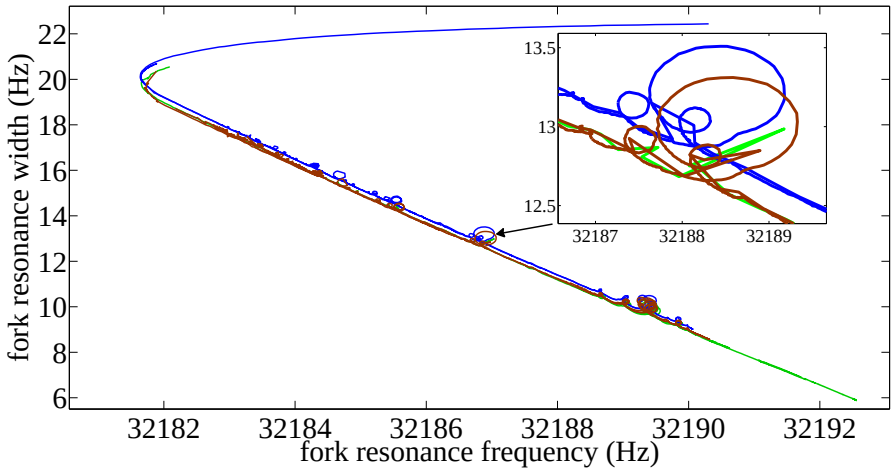

Figure 7.6: Three datasets obtained with pure ^{4}He during three different glass dewar cooldowns. Brown and light green data were obtained before measurements with any other ^{3}He concentration, and the blue data after them. In the light green dataset, the temperature sweep was continued to the lowest obtainable temperature, about 1.6 K. Inset shows a close up of one group of second sound resonances illustrating that some of the resonances are distorted in the light green dataset because the temperature sweep rate was too high during it.

The second sound resonances start already quite small in pure ^{4}He, but as the ^{3}He concentration is increased they first become even smaller and only after 2.1 % concentration their size starts to increase, eventually becoming very large compared to the starting point. Furthermore, as we noted, the lowest temperature resonances appear for the first time at 2.1 % concentration. The amplitude of the second sound resonances, *i.e.* the magnitude of the loop, is directly proportional to the coupling strength between second and first sound, as discussed in Section 3.1. In pure ^{4}He the coupling between second an first sound is already quite weak due to the small thermal expansion coefficient of superfluid helium. Then, as we add a small amount of ^{3}He, the coupling becomes even weaker, since the second term in brackets of eq. (3.32) has an opposite sign than the thermal expansion term. This is evident by the decreasing magnitude of the second sound resonances. When the second term begins do dominate, the coupling becomes stronger and stronger, and the magnitude of the second sound resonance loops starts to increase.

In fig. (7.7), we take a closer look of the region, where the second sound resonances first disappear, and then reappear, as the ^{3}He concentration is increased. This is the region where second sound and first sound decouple from each other. We have focused the view on those resonances that are clearly identifiable, and can therefore be followed through different concentrations. There

would be many more second sound resonances near T_λ, but their amplitude is always quite small and they are very close together making them very difficult to distinguish, especially when trying to find them at various concentrations. On the other hand, the lowest temperature resonances would very much stand out, but since they cannot be found in pure ^{4}He, they are not very useful in studying the decoupling region.

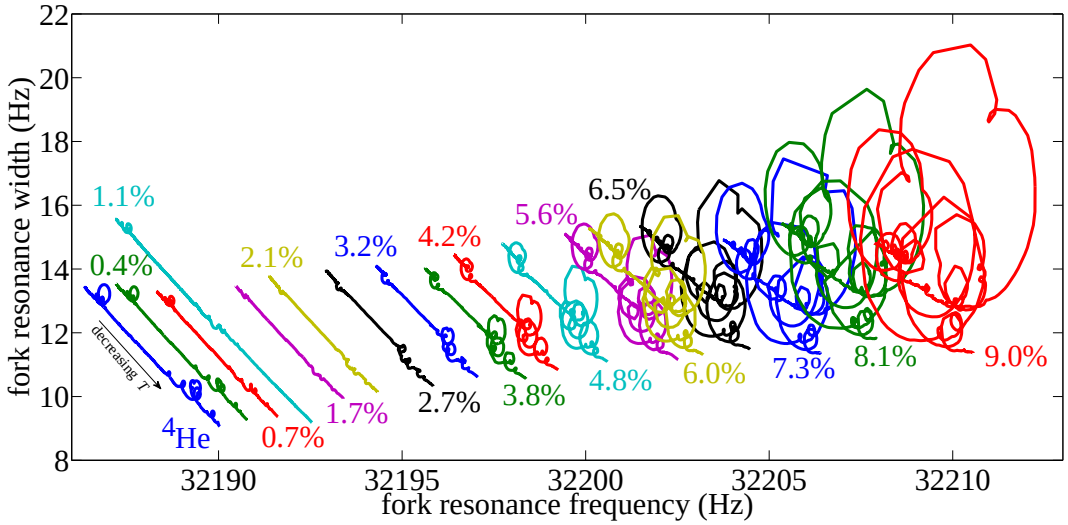

Figure 7.7: Cropped view of the region where the second sound resonances first disappear and then reappear as the ^{3}He concentration is increased. To make the figure clearer, the temperature sweeps up and the entire 11.0 % measurement have been omitted. The second sound resonances vanish between 1 % and 2 % concentrations, and reappear as the concentration is further increased.

Next, in fig. (7.8) we have focused the view on a single group of second sound resonances. In pure ^{4}He, this group can be found near 13 Hz fork resonance width. We have also numbered three of the second sound resonances that stand out clearly both before and after the sound mode decoupling. Before the decoupling, the second sound resonances are loops above the background slope, but afterward, just as they start to reappear, they are more like dints below the background level. Only as the ^{3}He concentration is increased even more, the loops start to become visible again, but their shapes are clearly different from those in pure ^{4}He. However, the second sound resonances still appear in the same order, the big resonance, labeled '2', is still between two smaller resonances in 4.2 % mixture, like it is in pure ^{4}He. Between 1.7 % and 3.2 % concentrations, it is slightly more difficult to recognize this resonance, since it has flipped below the background slope. Furthermore, we notice, that when we also take into account the temperature of the second sound resonances, the 1.1 % mixture dataset, that was clearly shifted in previous figures, seems to fit quite well with the other datasets.

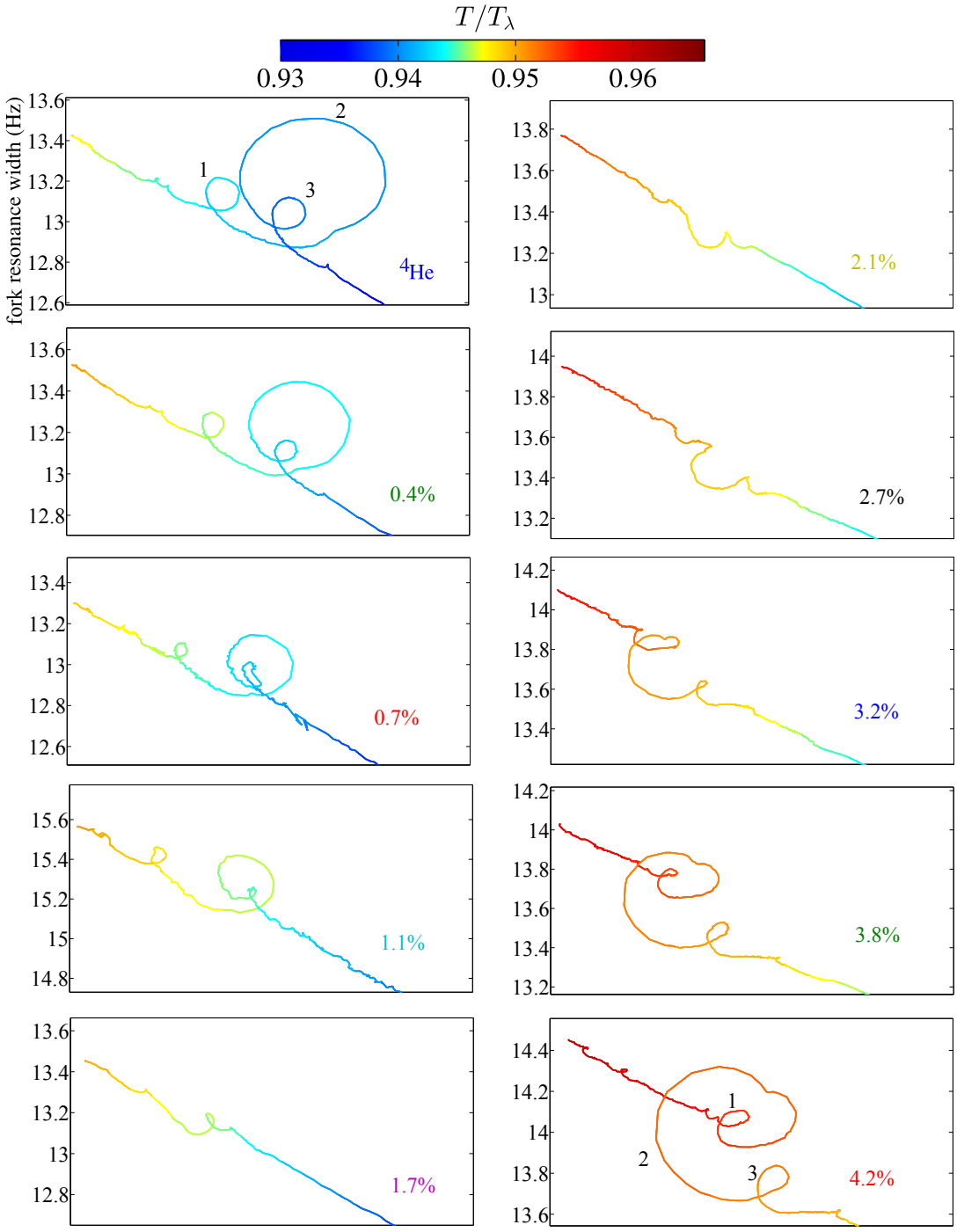

Figure 7.8: Closer view of the largest high temperature second sound resonance of fig. (7.7) followed through the decoupling region. The color of the line changes according to temperature, showing that the resonances move to a higher temperature as the ^{3}He concentration increases. Even though the shape of the resonances changes, we can still identify the three big resonances of pure ^{4}He also in 4.2 % mixture.

7.2 Constant Second Sound Velocity Curves

From figs. (7.7) and (7.8), we saw that it is possible to identify several equivalent second sound resonances from temperature sweeps at different ^{3}He concentrations, due to the resonances appearing in same sequence despite their changing amplitude and shape. These equivalent resonances form the same standing wave mode within the container of the quartz tuning fork, which is possible only if the velocity of the second sound remains constant. So, by following the second sound resonances it is possible to construct a constant second sound velocity plot.

We begin by looking at fig. (7.9), where we have plotted the observed second sound resonances in the plane of ^{3}He concentration and temperature relative to the λ-point. Note that the colors of fig. (7.9) are not related to the colors of previous figures. Now, the coloring points out an identified resonance followed through increasing ^{3}He concentrations. Not all followed resonances are indicated with colors, rather a few examples are pointed out in various temperature regions. Also, note that the 1.1 % dataset, that is clearly shifted in fig. (7.3), fits in quite well with other datasets in the relative temperature presentation, although it is still missing the small second sound resonances near the λ-point, as its temperature sweep rate was too high there.

The sound decoupling region is also visible in this plot, and we actually see some temperature dependence in it. The amplitude of the second sound resonances near T_λ is smallest at higher concentration than the amplitude of the resonances at lower temperatures.

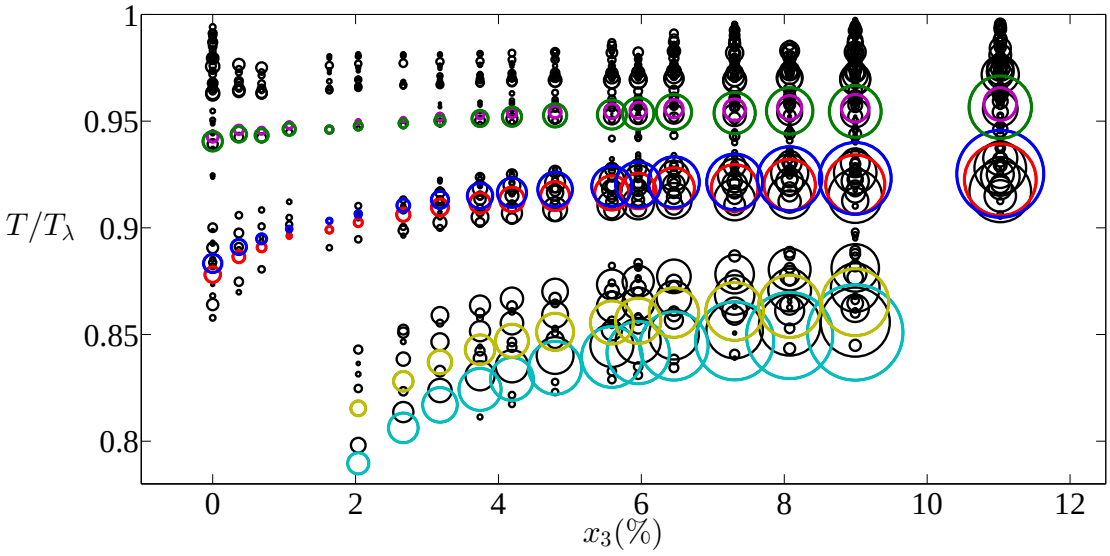

Figure 7.9: Observed second sound resonances in the plane of ^{3}He concentration and temperature relative to the superfluid transition temperature T_λ. The amplitude of the resonance is represented by the size of the circle. The coloring indicates examples of the same resonance followed through different concentrations.

The second sound resonances were identified, and followed, from frequency-width plots, while their amplitude and location in temperature space was determined from temperature-width presentations, such as the one shown in fig. (7.2). Since we measured only pure ^{4}He during multiple cooldowns, we have to rely on its data to evaluate the error in the resonance location. When we evaluate the location error using pure ^{4}He runs, from multiple cooldowns, we end up with a value $\pm 3\,\mathrm{mK}$, or about $\pm 0.0014 T_\lambda$. Conversely, the error between temperature sweep down and temperature sweep up, in a single cooldown, is merely $\pm 0.6\,\mathrm{mK}$. The error in the ^{3}He concentration is ± 0.3 percentage points, as discussed earlier.

Next, in fig. (7.10), we have a constant second sound velocity plot, obtained using the equations discussed in Sections 3.1 and 3.3. Then, in fig. (7.11), we essentially have the same data as in fig. (7.9), but now we show only those second sound resonances we were able to identify and follow through different ^{3}He concentrations, we have also left out the circles representing the amplitude of the resonance. Lastly, in fig. (7.12) we have superimposed the two previous figures to make comparison easier.

When we compare the contours of these two plots, we see that they behave similarly. Near the λ-point, as we go from concentration to concentration, we can find the same resonance practically at same relative temperature. Correspondingly, in the same region, the constant second sound velocity curve is almost horizontal. When we move to a lower temperature, the resonance locations at higher concentrations are still about constant in relative temperature, but at lower concentrations the observed resonances start to arc towards lower temperatures, which is again mirrored by the constant second sound velocity curves. Finally, the behavior of the constant velocity would also explain why we cannot locate the lowest temperature second sound resonances in pure ^{4}He. The constant second sound velocity has, in fact, curved so much that it no longer intersects the 0 % line. However, there are some differences between the two as well: at higher ^{3}He concentrations, there is still a clear slope in the constant second sound velocity in the calculated model, whereas in the measured data the slope is noticeably smaller. Our calculated model is valid at low concentrations, meaning we should not use it to make any serious assumptions how the constant second sound velocity would behave at increasing ^{3}He concentrations. Furthermore, near the decoupling region, the amplitude of the second sound resonances becomes very small, which makes them difficult to identify.

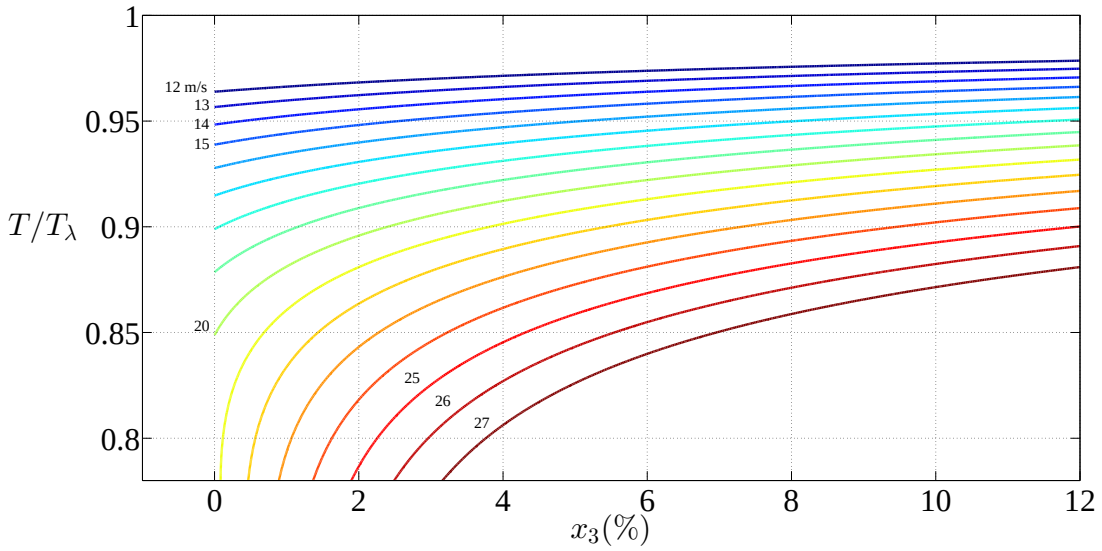

Figure 7.10: Calculated constant second sound velocity curves in the plane of ^{3}He concentration and temperature relative to the superfluid transition temperature, T_λ. The velocity values in m/s are shown next to the curves.

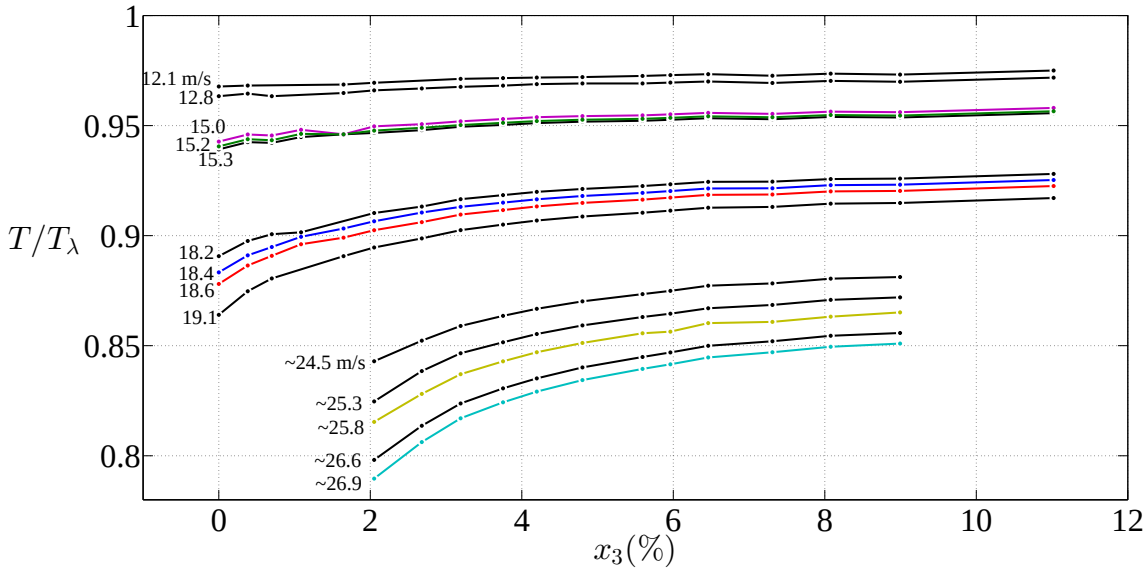

Figure 7.11: Constant second sound velocity curves obtained by following the second sound resonances through different concentrations. The second sound velocity values, in m/s, are shown by the numbers next to the curves. The values indicated by " $\sim$ " were evaluated from our calculated model, while the others were obtained from the pure ^{4}He second sound velocity data by Donnelly and Barenghi [18]. The colors here match the colors of the resonances in fig. (7.9).

The strong resemblance between the figs. (7.10) and (7.11) confirms that we have followed the second sound resonances correctly, which could have been called to question, as the identification of the resonances was basically done by eye. The constant second sound velocity value, for those resonances that are also found in pure ^{4}He, can be obtained from various sources, as the second sound velocity in pure ^{4}He is well known. But for the resonances that did not appear in pure ^{4}He, the velocity values had to be taken from our calculated model, which makes them more unreliable. Below $u_2 = 20\,\frac{\mathrm{m}}{\mathrm{s}}$, our calculated model gives roughly 10 % larger second sound velocity than the value obtained from pure ^{4}He velocity data of Donnelly and Barenghi [18].

The constant second sound velocity curves obtainable with this kind of measurement are restricted to regions where there actually are second sound resonances. For example, in our data, there are gaps between $15.3\,\frac{\mathrm{m}}{\mathrm{s}}$ and $18.2\,\frac{\mathrm{m}}{\mathrm{s}}$, and between $19.1\,\frac{\mathrm{m}}{\mathrm{s}}$ and $24.5\,\frac{\mathrm{m}}{\mathrm{s}}$, simply because there are no second sound resonances there. To get a more complete dataset, the measurement would have to be done with several different forks, which would have second sound resonances at different temperatures. In this sense, too, it would have been very useful if our 40 kHz fork had worked properly.

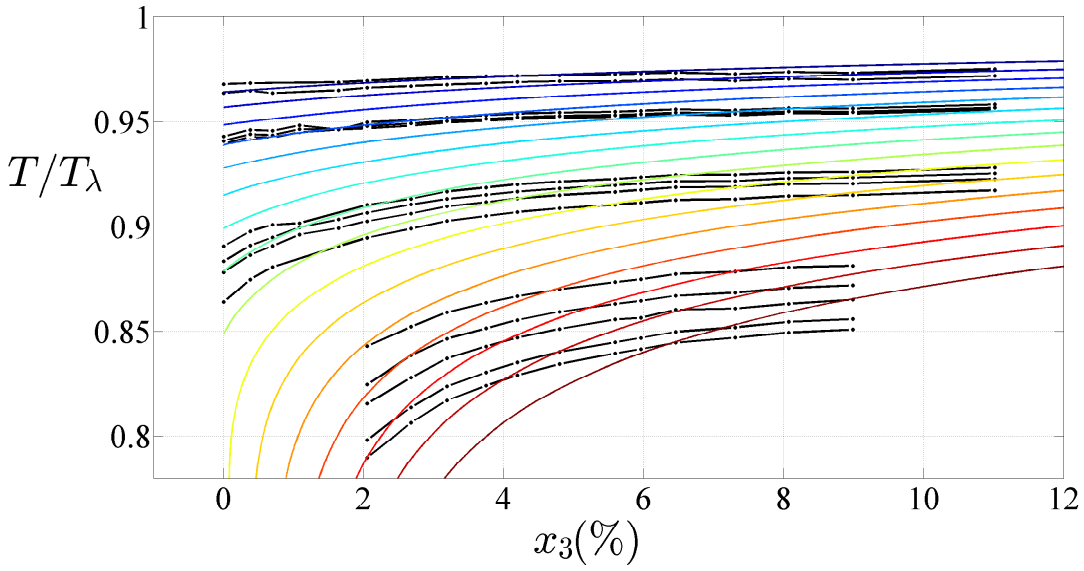

Figure 7.12: Comparison between the calculated constant second sound contours of fig. (7.10), and the measured data of fig. (7.11). Discrepancy between the calculated model and measured data becomes larger at lower temperatures and higher concentrations.

7.3 Amplitude of the Second Sound Resonances and Coupling Factors

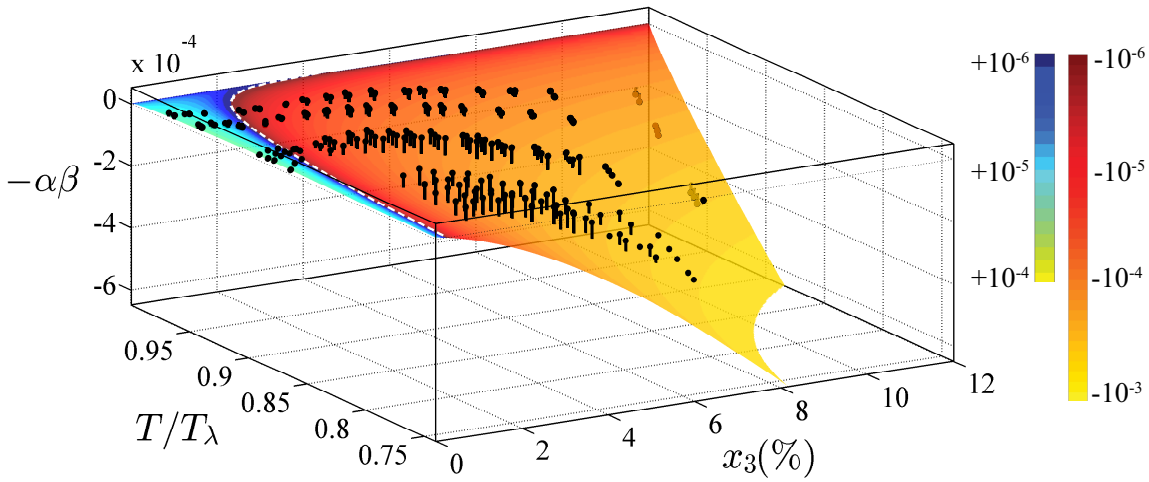

Figure 7.13: Plotted surface is the result of the theoretical calculation of the product of the coupling factors, $-\alpha\beta$, as a function of ^{3}He concentration and temperature relative to the λ-point, whereas the stems are the measured amplitudes of the second sound resonances normalized to the 9.0 % ^{3}He concentration calculated data. The length of the stem is the difference between the calculated and the measured value. The z-axis is linear, but the colormap of the surface is logarithmic in order to emphasize the decoupling region. Surface is semitransparent to make the stems that lie beneath it visible. Dashed white line indicates where $\alpha = 0$ according to our calculated model.

The most important thing we learned of the coupling between second and first sound is already clearly visible from the fork's frequency-width plots of Section 7.1: there is a region, around 1 % ^{3}He concentration, where second sound resonances vanish as the two sound modes decouple from each other, and second sound can no longer generate first sound. In this section, we want to compare the observed amplitude of the second sound resonances to the calculated strength of the coupling, represented either by the product of the coupling factors $\alpha\beta$, in the case of double sound conversion, or by justα, in single sound conversion, as discussed in Section 3.2.

In our data analysis, we have assumed that the coupling strength is proportional to the product of the coupling factors. Using equations (3.30) and (3.32) it is possible to construct a surface to represent the product, $\alpha\beta$, as a function of ^{3}He concentration, and relative temperature T/T_λ. To make comparison with the second sound resonance data possible, we have normalized the resonance amplitude to the $\alpha\beta$ value at 9.0 % concentration, so at this concentration calculated data and measured data match exactly. The second sound resonances, that can be normalized to the amplitude value at some specific ^{3}He concentration, are those same resonances, we were able to follow through different concentrations in fig. (7.11).

The comparison plot is shown in fig. (7.13). We have plotted the surface as $-\alpha\beta$ to make the measured datapoints more visible. While the z-axis of this plot is linear, the colormap of the surface

is base 10 logarithmic to make the decoupling region stand out. Since the second sound resonance amplitude data do not contain any information about the sign of the product of the coupling factors, we have manually inserted it to match the calculated data. Before the decoupling, below about 1 % concentration, the product is positive, while after the decoupling, it is negative. The amplitude data is presented in a stem plot, where the dot indicates the data point, and the line the distance from the calculated surface. Overall, the measured data behaves very similarly to the calculated data, though our data points are systematically above the surface, except for the 11.0 % dataset, which lies mostly below the surface. The temperature sweep rate of the 11.0 % measurement was somewhat faster than in the other measurements, which could distort the resonances causing error in their amplitude determination. The observed coupling then generally seems to be stronger at low concentrations than our calculated model predicted, but at high concentrations it is the other way around. Our calculated model assumed, for example, an ideal solution of ^{3}He and ^{4}He, where the components do not interact with each other. This could result in our model underestimating the effect ^{3}He has to the the coupling strength. Additionally, the only dataset lying almost completely below the surface is the one at a larger concentration than the 9.0 % normalization concentration, implying that the normalization already may have skewed the measured data. When we are normalizing the the amplitudes of the set of resonances followed through different ^{3}He concentration to the amplitude value at a single concentration, we are implicitly assuming that the rest of the second sound resonances in the set have the same quality factor, which, in reality, is a function of temperature and concentration, which would have to be taken into account to get more accurate comparison between the measured and the calculated data.

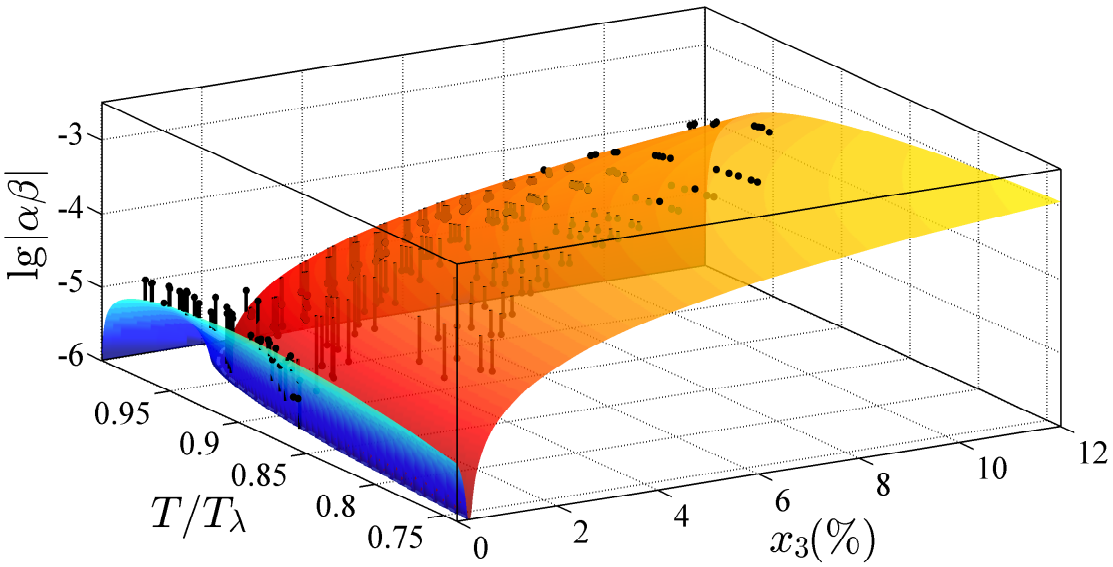

Figure 7.14: Same data as in fig. (7.13), but with logarithmic z-scale.

To emphasize the decoupling region even more, in fig. (7.14), we have also set the z-axis to logarithmic scale, but we have kept the same colormap as before. The decoupling region now clearly stands out as a ravine, and we also see how the surface curves to zero when approaching the λ-point. At T_λ the product of the coupling factors becomes zero since the superfluid density goes to zero.

The measured data still seems to match calculated data quite well. However, the length of the stems near the decoupling region indicates that we had reached the resolution of our quartz tuning fork measurement there. This is shown more clearly in the relative residual plots of fig. (7.15), where the residuals are noticeably larger near the decoupling region, and their sign changes more often than in the measurements at higher concentrations. If we were able to make a mixture with concentration even closer to the decoupling concentration, it would become even more difficult to separate the miniscule second sound resonances from the background noise.

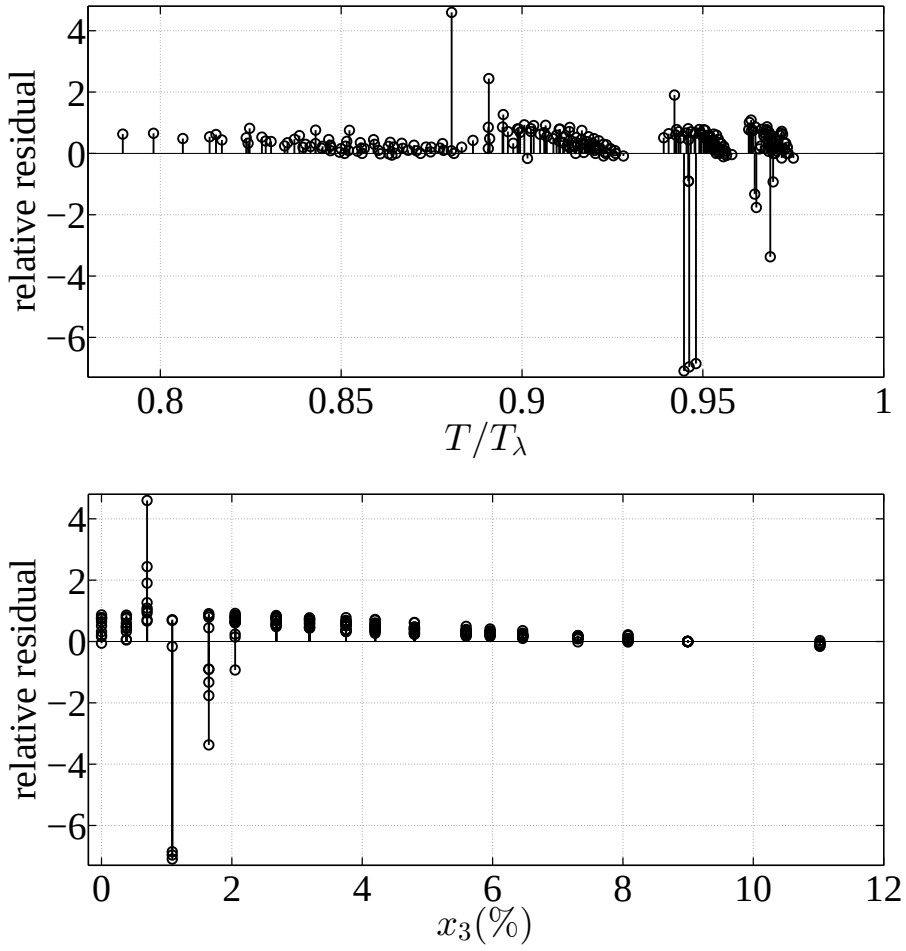

Figure 7.15: Relative residual (difference between measured data point and corresponding point on the calculated surface, divided by the value at the surface) as a function of relative temperature (upper), and ^{3}He concentration (lower).

Because the coupling factor between first and second sound, β, shown in fig. (3.6), is small, always non-zero, and almost constant everywhere except very close to T_λ, its contribution to the product $\alpha\beta$ is very difficult to observe. In fact, we can leave β out of this surface analysis, and normalize the measured data only to the coupling factor between second and first sound, α, without greatly diminishing the consistency between the calculated model and the measured data. Our experiment then cannot tell whether the first sound that couples back to the fork is created by a single sound conversion from second sound generated by the fork, or by a double sound conversion from first sound generated by the fork. But in either case we get information about the coupling factor α, as it alone determines the decoupling behavior. In order to get more information about the small coupling factor β, we could repeat our measurement at higher pressures, where the compressibility of helium would change its behavior and maybe make it more easily observable.

Next, in fig. (7.16), we look at the previous surface plots from above, on the plane of ^{3}He concentration and relative temperature T/T_λ. At low temperature, the decoupling is predicted to occur already at about 0.3 % concentration, and as the temperature increases the decoupling concentration also increases to about 1 % in the region where most of our observable second sound resonances were, and finally going somewhere above 4 % concentration as we get closer to T_λ. Naturally, as we approach the λ -point, the product of the coupling factors goes to zero at any ^{3}He concentration, as the superfluid density goes to zero at T_λ.

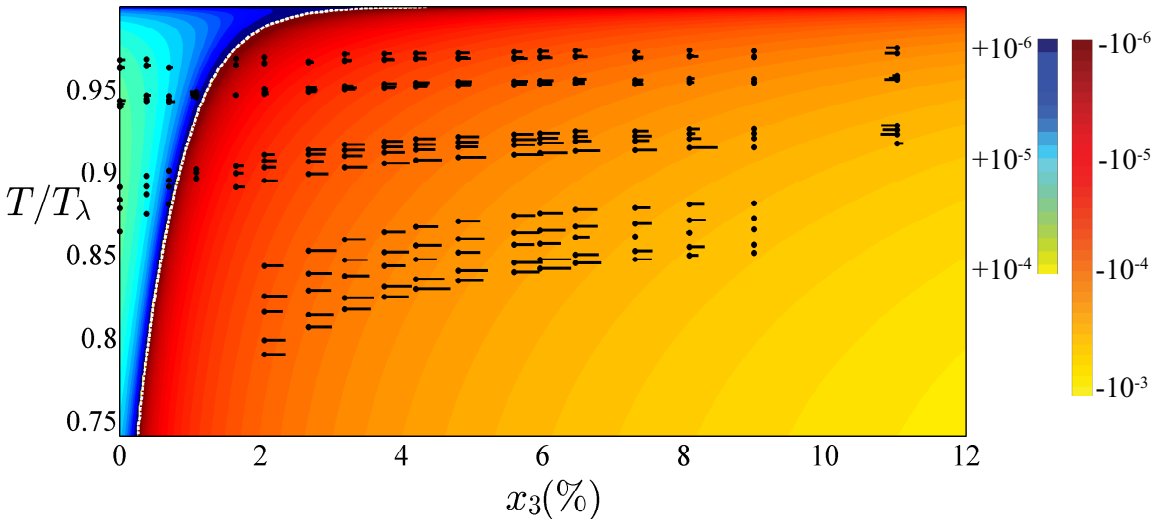

Figure 7.16: Projection of the calculated surface in the plane of ^{3}He concentration and temperature relative to the superfluid transition temperature T_λ. Even though the stems are parallel to the x-axis in this presentation, they still represent the difference between the datapoint and the surface in the z-direction. When the line of the stem is on the right side of the datapoint, the datapoint is above the surface, and when it is on the left side, the datapoint is below the surface.

Finally, in fig. (7.17), we compare the decoupling region obtained from our measurements to the $\alpha = 0$ line calculated in Section 3.3 (see fig. (3.5)). By making a linear fit to each set of followed second sound resonances, both before and after the decoupling, we can evaluate the decoupling temperature and concentration as the intersection point of the two lines. Then, to evaluate error, we can pick a set of resonances before the decoupling region, which clearly have larger than zero amplitude, and similarly after the decoupling region. The error estimated this way is shown as the shaded areas in fig. (7.17). Decoupling seems to occur at higher concentrations than predicted by our calculated model. This is likely mostly due to the approximations made in our calculated model, but also at least partly due to the linear fit oversimplifying the behavior of the resonances near the decoupling region.

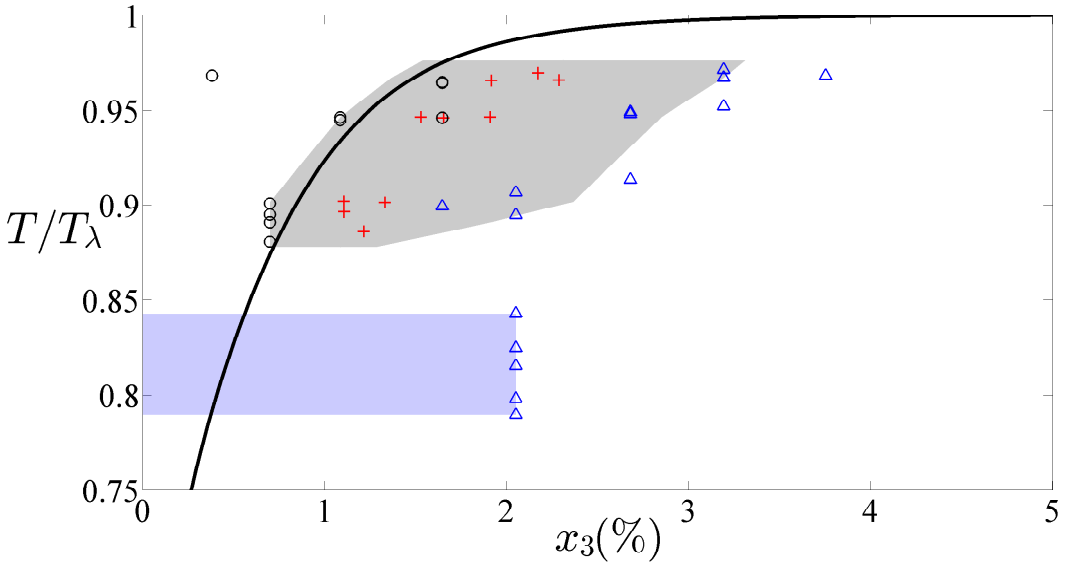

Figure 7.17: Comparison between $\alpha = 0$ line obtained from our calculations (solid line), and the measured region where the second sound resonances disappear in the plane of ^{3}He concentration and relative temperature. Here ($\circ$) indicates the locations, where the resonances clearly had not disappeared yet, and ($\triangle$) the locations where they had reappeared. Locations marked by ($+$) are the evaluated decoupling points obtained by making a linear fits to the experimental data both sides the decoupling region. Shaded areas indicate the confidence bounds of the measured decoupling region. Since the low temperature resonances do not appear in pure ^{4}He, their error bound extends to 0 % concentration.

8 Discussion

The goal of our experiment was to observe coupling between first and second sound in dilute ^{3}He – ^{4}He mixtures, using a quartz tuning fork oscillator, at temperatures available with ^{4}He evaporation cooling, and to confirm whether there exists a region where the second and first sound decouple from each other. The main result was clearly visible already from practically raw measurement data. The amplitude of the second sound resonances first decreased with increasing ^{3}He concentration until about 2 % mixture, after which the amplitude started to increase, which is evidence of the decoupling behavior. Additionally, we noticed that after the decoupling region, there appeared new resonances at low temperatures that were not visible in the most dilute mixtures. We compared the amplitude of the second sound resonances to calculated values of the product of the coupling factors, and found that they were generally consistent, both near the decoupling region and farther away from it, but the decoupling occurs at slightly higher concentration than predicted by the calculations.

Furthermore, the second sound resonances were sufficiently unique, making it possible to find equivalent resonances in different concentrations. These resonances formed constant second sound velocity curves, which also were in good agreement with the corresponding calculated data.

Initial plan was to use two quartz tuning forks with different resonance frequencies, but the locations of the second sound resonances were not properly reproducible in one of them. It would have been more thorough to verify the decoupling of the second and first sound using two different forks, with two different sets of second sound resonances. Using two forks, we also could have obtained a few more constant second sound velocity curves, which could have filled the velocity gaps in fig. (7.11). However, the decoupling temperature and concentration should not depend on the quartz tuning fork, as it is a property of the medium not the oscillator. Only the exact locations of the second sound resonances are fork dependent, because each fork container has unique standing wave patterns.

In the 32 kHz fork, the locations of the second sound resonances remained fairly constant in temperature between different cooldowns, which we estimated within ± 3 mK. There is a much larger uncertainty in the absolute temperature values of the resonance locations, since there is already clear discrepancy between T_λ determined from our measurements and values found in other publications, as seen in fig. (7.4). Nevertheless, the error caused by this is somewhat diminished as we present our data in temperature scale relative to the superfluid transition temperature. The error in ^{3}He concentration determination was relatively larger than in temperature determination, as it was mainly due to the uncertainty of our calibration mixtures.

One application for the second sound resonances could be in indicating some fixed point in temperature. If we could once somehow determine precisely the temperature of a second sound resonance appearing in the quartz tuning fork response, we would know, that the next time we saw it, the temperature would be the same with very good accuracy. Another way to utilize the second sound resonances would be to use them to help keep an experiment at a constant temperature. In our experiment, we used PID controlled heater, which was reading the resistance value of a carbon

resistor thermometer, to control temperature of the ^{4}He bath. It works well in temperature sweeps, but if we would try to keep the temperature constant, it would not be the most accurate method since the resistance value drifts somewhat. But, if we were to instead have the PID controlled heater follow a second sound resonance by reading the fork resonance width, for example, we could be sure that the temperature is truly constant. To get an idea of the temperature range, let us say we manage to fix our temperature so that we are always within half width of a second sound resonance, for instance, the first small resonance loop in pure ^{4}He dataset in fig. (7.8), the one at roughly 13 Hz fork resonance width. The temperature difference between the beginning and the end of the loop is about 2 mK, so we could potentially keep the temperature constant with that accuracy. As we lower the temperature, the second sound resonances spread wider in temperature decreasing the accuracy of the constant temperature. However, if we could find a second sound resonance with sufficient fine structure, caused by having several resonances close together, we could fix our temperature controller on them narrowing down the temperature spread.

We actually tried to make our PID controller follow a single second sound resonance, but there were essentially two problems: first, since the glass dewar was not properly insulated from its surroundings, the heat load to its ^{4}He bath fluctuated quite strongly, and secondly, our PID controller simply was not fast enough to adjust the current to the heating resistor to compensate the external heat load within such a small temperature range. In order to study the possibility of this temperature control application properly, we would have to change our experimental setup considerably.

A natural continuation to our experiment would be to add pressure to the variables, while now we did all the measurements under saturated vapor pressure. We could study, if increasing pressure would considerably change the appearance of the second sound resonance loops, and if it would change the behavior of the decoupling region. Varying pressure could also tell us more about the coupling factor β, which is nearly constant under saturated vapor pressure. Another way to continue would be to go to even lower temperature, to go to the other side of the second sound velocity maximum in mixtures. The temperature regime of that experiment would be below 1 K, which is not reachable using evaporative cooling of ^{4}He, but we would have to use a different cooling method, a dilution refrigerator, for example. Furthermore, near the decoupling region, we noticed that the second sound resonances had "flipped over", compared to pure ^{4}He resonances. We could try to gain better understanding of it by doing simulations with coupled oscillators, and study if they had any similar behavior with certain parameters.

List of Symbols

α	coupling factor between second and first sound
β	coupling factor between first and second sound
c	mass concentration of ^{3}He
f_0	quartz tuning fork resonance frequency
f	quartz tuning fork measurement frequency
$\mathbf{j}$	mass flux
κ	thermal expansion coefficient
μ	specific chemical potential
$\mu_4\,(\mu_3)$	specific chemical potential of ^{4}He $(^3$He$)$
$m_4\,(m_3)$	atomic mass of ^{4}He $(^3$He$)$
m_3^*	effective mass of ^{3}He
$M_4\,(M_3)$	molar mass of ^{4}He $(^3$He$)$
n_4	number density of ^{4}He
n_4^0	number density of ^{4}He at absolute zero, at zero pressure
$N_4(N_3)$	number of ^{4}He $(^3$He$)$ atoms
ξ	normal fluid fraction of pure ^{4}He
P	pressure
R	molar gas constant
ρ	total density
$\rho_\mathrm{n}\,(\rho_\mathrm{s})$	normal fluid (superfluid) density
σ	specific entropy
$\sigma_{40}\,(\sigma_{30})$	specific entropy of pure ^{4}He $(^3$He$)$
t	time
T	temperature
T_λ	superfluid transition temperature of ^{4}He

u_1	velocity of first sound
u_2	velocity of second sound
$\mathbf{v}_\mathrm{n}$ ($\mathbf{v}_\mathrm{s}$)	normal fluid (superfluid) velocity
V	voltage
V_m ($V_{\mathrm{m},4}$)	molar volume (pure ^{4}He)
ω	angular frequency
w	quartz tuning fork resonance width
x_3	molar concentration of ^{3}He

References

[1] H. Kamerlingh Onnes. *The Liquefaction of Helium.* Proc. KNAW., **11**, 168–185 (1909).

[2] J. Bardeen, L. N. Cooper, and J. R. Schrieffer. *Theory of Superconductivity.* Phys. Rev., **108**, 1175–1204 (1957).

[3] F. Pobell. *Matter and Methods at Low Temperatures*, (Springer, 2007), 3 ed.

[4] P. Brusov, J. M. Parpia, P. Brusov, and G. Lawes. *Sound conversion in impure superfluids.* Phys. Rev. B, **63**, 140507(R) (2001).

[5] J. Rysti. *Microscopic and Macroscopic Studies of Liquid and Solid Helium Mixtures.* Ph.D. thesis, Aalto University School of Science, O. V. Lounasmaa Laboratory (2013).

[6] J. T. Tuoriniemi et al. *Towards Superfluidity of* ^{3}He *Diluted by* ^{4}He. J. Low Temp. Phys, **129**, 531–545 (2002).

[7] L. Tisza. *Transport Phenomena in Helium* II. Nature, **141**, 913 (1938).

[8] L. Tisza. *The Theory of Liquid Helium.* Phys. Rev., **72**, 838–854 (1947).

[9] L. Landau. *Theory of the Superfluidity of Helium* II. Phys. Rev., **60**, 356–358 (1941).

[10] I. M. Khalatnikov. *An Introduction to the Theory of Superfluidity*, (Westview Press, 2000).

[11] J. Wilks. *Liquid and Solid Helium*, (Clarendon Press, 1967).

[12] D. R. Tilley and J. Tilley. *Superfluidity and Superconductivity*, (Van Nostrand Reinhold Company Ltd, 1974).

[13] T. R. Roberts, R. H. Sherman, S. G. Sydoriak, and F. G. Brickwedde. *The 1962* ^{3}He *Scale of Temperatures.* Prog. Low Temp. Phys., **4**, 480–514 (1964).

[14] H. C. Kramers, J. D. Wasscher, and C. J. Gorter. *The Specific Heat of Liquid Helium between 0.25 and 1.9 K.* Physica, **18**, 329–338 (1952).

[15] R. W. Hill and O. V. Lounasmaa. *The specific heat of liquid helium.* Phil. Mag,, **2**, 143–148 (1957).

[16] G. Baym and C. Pethick. *Low Temperature Properties of Dilute Solutions of* ^{3}He *in Superfluid* ^{4}He. The Physics of Liquid and Solid Helium Part II, **29**, 123–176 (1978).

[17] M. S. Manninen. *Oscillations on helium surfaces.* Ph.D. thesis, Aalto University School of Science, Department of Applied Physics, Low Temperature Laboratory (2015).

[18] R. J. Donnelly and C. . F. Barenghi. *The Observed Properties of Liquid Helium at the Saturated Vapor Pressure.* J. Phys. Chem. Ref. Data, **27**, 1217–1274 (1998).

[19] E. R. Dobbs. *Helium Three*, (Oxford University Press, 2000).

[20] J. J. Niemela and R. J. Donnelly. *Density and Thermal Expansion Coefficient of Liquid Helium-4 from Measurements of the Dielectric Constant.* J. Low Temp. Phys, **98**, 1–16 (1995).

[21] E. Pentti et al. *Studies on Helium Liquids by Vibrating Wires and Quartz Tuning Forks.* J. Low Temp. Phys., **165**, 132–165 (2011).

[22] C. T. Lane, H. A. Fairbank, and W. M. Fairbank. *Second Sound in Liquid Helium II.* Phys. Rev., **71**, 600–605 (1947).

[23] R. D. Maurer and M. A. Herlin. *Second Sound Velocity in Helium II.* Phys. Rev., **76**, 948–950 (1949).

[24] D. de Klerk, R. P. Hudson, and J. R. Pellam. *Second Sound Propagation below 1 K.* Phys. Rev., **93**, 28–39 (1954).

[25] J. C. King and H. A. Fairbank. *Second Sound in* He^3 - He^4 *Mixtures below 1 K.* Phys. Rev., **93**, 21–28 (1954).

[26] N. R. Brubaker et al. *The Velocity of Second Sound in Dilute* ^{3}He - ^{3}He *solutions below 0.6 K.* J. Low Temp. Phys, **3**, 619–634 (1970).

[27] T. R. Roberts and S. G. Sydoriak. *Sound Velocity, Phase Separation and Lambda Transitions of* He^3 - He^4 *Mixtures.* Phys. Fluids, **3**, 895–902 (1960).

[28] R. Blaauwgeers et al. *Quartz Tuning Fork: Thermometer, Pressure- and Viscometer for Helium Liquids.* J. Low Temp. Phys, **146**, 537–562 (2007).

[29] J. T. Tuoriniemi, J. Rysti, A. Salmela, and M. S. Manninen. *Mode Analysis for a Quartz Tuning Fork Coupled to Acoustic Resonances of Fluid in a Cylindrical Cavity.* J. Phys: Conf. Ser., **400**, 1–4 (2012).

[30] K. W. Taconis and R. D. B. Ouboter. *Equilibrium Properties of Liquid and Solid Mixtures of Helium Three and Four.* Prog. Low Temp. Phys, **4**, 38–96 (1964).